



University of  
**BRISTOL**

School of Chemistry

## Beta Enhanced Thermionic Emission

Alexander Rowan

Supervisor: Dr. Neil Fox

Second Assessor: Prof. Paul May

*A thesis submitted in partial fulfilment of the requirements for the MSci  
Honours Degree in Chemistry*

April 2017

# Abstract

Thermionic energy converters (TECs) have the potential to improve the efficiency of power generation by converting heat directly to electrical energy. This report examines beta irradiation as a method of improving the process of thermionic emission.

Nitrogen doped nanocrystalline diamond (NDNCD) grown on molybdenum substrates, was used as an emitter. Its high thermal stability and radiation hardness made NDNCD an optimal n-type semiconductor for this project. The energy barrier for emission was lowered by terminating the surface with hydrogen which produced a negative electron affinity (NEA). The thermionic properties of the emitter were then studied by radiatively heating the sample with a 40 W CO<sub>2</sub> laser under vacuum. Beta irradiation was provided by a 2.6 MBq <sup>63</sup>Ni source.

At temperatures above 600 °C the terminated NDNCD produced an emission of the order of 100 μA cm<sup>-2</sup>. The hydrogen termination was unstable at elevated temperatures, causing depletion of the NEA and raising the energy barrier of emission over the course of the emitters operation. In spite of this, beta irradiation of the emitter consistently produced an emission enhancement of over 100%.

Further research is necessary to explain the magnitude of this enhancement but it is suggested, as a working hypothesis, that this was caused by electron-hole pair generation, enhancing the conductivity of the n-type semiconductor. It is also theorised that trap passivation improved the conductivity of the semiconductor bulk.

## Acknowledgements

I would like to thank Dr. Neil Fox for his vital insight, encouragement and support in my final year, Prof. Paul May, who has created an extraordinary academic environment in the Diamond lab and James Smith for his tireless and selfless assistance with every aspect of my project.

My thanks also goes to Douglas Mills, Adrian Crimp and John Rowden from the Chemistry and Physics workshops. Their innovative solutions to practical problems greatly facilitated the completion of this project.

Lastly, I would like to thank all the members of Diamond lab for the encouragement they consistently provided. Special mention must go to Gary Wan, for his help understanding the TEC equipment, Hugo Andrade, for his invaluable aid in deciphering the myriad of phenomena found during my investigation and Alexander Croot, whose strength and guidance has enabled me, in large part to produce this report.

# Contents

<b>Abstract</b>	I
<b>Acknowledgements</b>	II
<b>Contents</b>	III
<b>1 Introduction</b>	
1.1 Thermionic Emission	
1.1.1 History	- 1 -
1.1.2 Theory	- 1 -
1.2 Thermionic Energy Converters	
1.2.1 Overview	- 2 -
1.2.2 Applications	- 3 -
1.2.3 Practical Limitations of TECs	- 4 -
1.3 Diamonds	
1.3.1 History	- 5 -
1.3.2 Properties	- 5 -
1.3.3 Synthesis	- 6 -
1.3.4 Doping	- 8 -
1.3.5 Surface Morphology & Termination	- 10 -
1.4 Beta Enhanced Thermionic Emission (BETE)	- 14 -
<b>2 Experimental</b>	
2.1 Overview	- 15 -
2.2 Equipment	
2.2.1 Emitter	- 15 -
2.2.2 Collector	- 19 -
2.2.3 TEC	- 20 -
2.3 Methodology	
2.3.1 Profile	- 23 -
2.3.2 Run	- 24 -
<b>3 Results</b>	
3.1 Thermionic Emission	
3.1.1 Emission Profile	- 25 -
3.1.2 Emission Run	- 27 -
3.2 Beta Enhanced Thermionic Emission	
3.2.1 Overview	- 31 -
3.2.2 Hypotheses	- 34 -
3.3 Emission Threshold	- 36 -
3.4 Trap Passivation Effect	
3.4.1 Theory	- 37 -
3.4.2 Experimental	- 38 -
3.4.3 Results	- 39 -
<b>4 Conclusion</b>	
4.1.1 Summary	- 41 -
4.1.2 Future Work	- 41 -
<b>6 Bibliography</b>	- 43 -

# 1 Introduction

## 1.1 Thermionic Emission

### 1.1.1 History

Thermionic emission was proposed by Owen Richardson, at the start of the 21<sup>st</sup> century, as an explanation for the atmospheric charging that occurred around a heated wire filament. He proposed that thermal excitation of a material can raise the energy of its electrons above that of the vacuum level, causing electrons to be emitted from the surface. The theory was widely accepted and Richardson won the Nobel Prize in physics for his work in 1928.

### 1.1.2 Theory

The evaporation of electrons from the surface of an emitter is described by the Richardson-Dushman equation. The emission current density,  $J(T)$ , is described as a function of the temperature,  $T$ , the work function,  $\phi$ , and the Richardson Constant,  $A_R$ .

$$J(T) = A_R T^2 e^{-\frac{\phi}{k_B T}} \quad (1)$$

The ideal Richardson constant,  $A_0$ , does not account for the differing surface properties of the emitter. A surface dependant modifier,  $\lambda_R$ , is used to account for the varying morphology, electric fields and conductivity of each emitter.

$$A_R = A_0 \lambda_R \quad (2)$$

The ideal theoretical value,  $A_0$ , is calculated as  $123 \text{ A cm}^{-2} \text{ K}^{-2}$ . It is determined by the electron effective mass,  $m_e$ , Boltzmann's constant,  $K_B$ , charge of an electron,  $e$ , and Planck's constant,  $h$ .

$$A_0 = \frac{4\pi m_e K_B^2 e}{h^3} \quad (3)$$

## 1.2 Thermionic Energy Converters

### 1.2.1 Overview

The concept of thermionics as a method of direct energy conversion has existed for over a century.<sup>1</sup> Thermionic energy converters (TECs) use thermionic emission to radiate high energy excited electrons from a hot emitter. A cold collector gathers these electrons creating a charge difference between these two electrodes. If the anode and the cathode are connected the potential difference will induce a current, allowing work to be done (Figure 1).

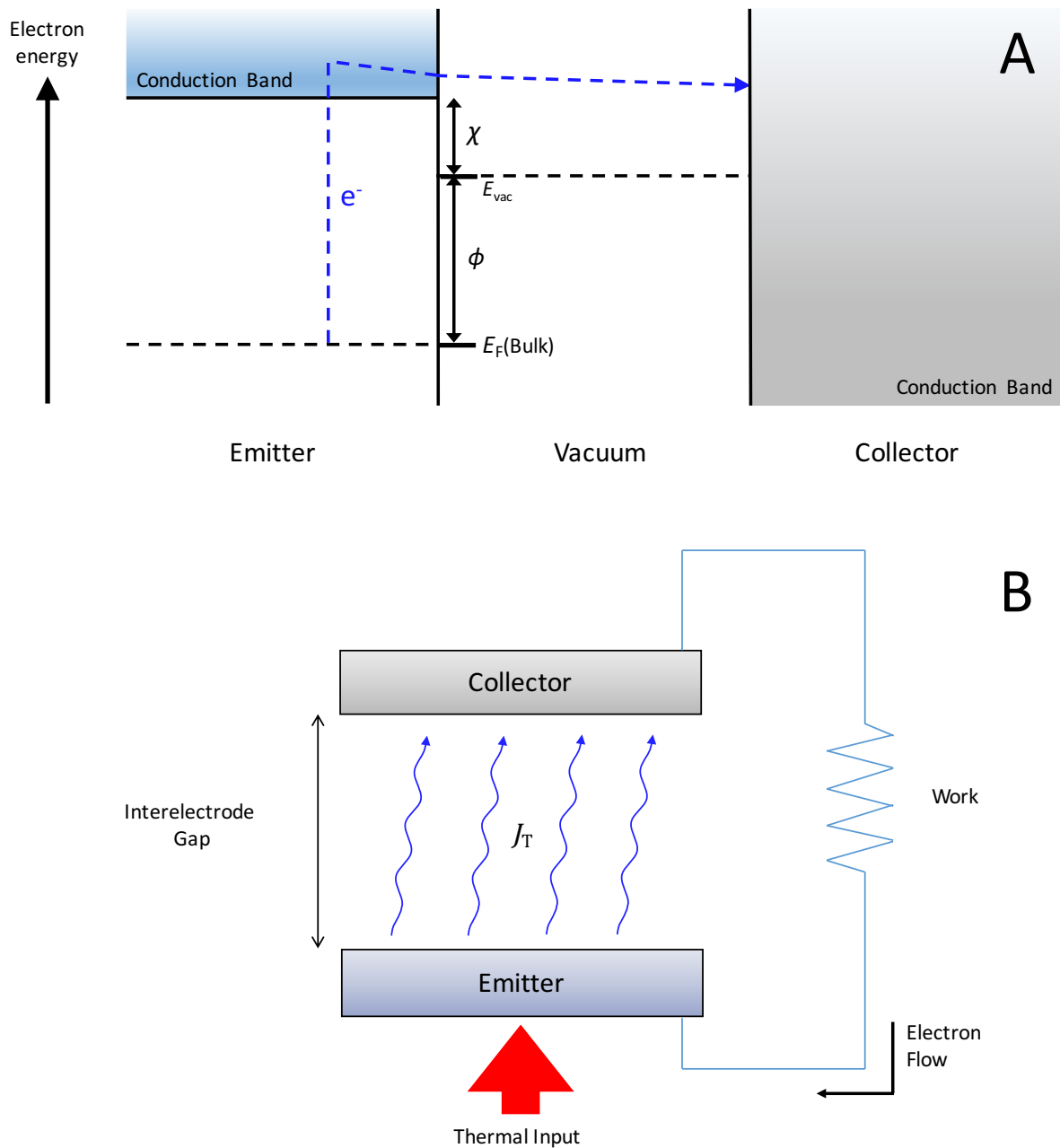


Figure 1: Energy diagram (A) and Schematic (B) of a TEC. In A, the electron affinity,  $\chi$ , is the energy difference between the conduction band minimum and the energy of a free stationary electron in the vacuum,  $E_{vac}$ . The Fermi level of the semiconductor is denoted by  $E_F$ .

As with all heat engines, the efficiency of TECs is limited by the Carnot cycle (Equation 4). The efficiency of the Carnot cycle is maximised by a large temperature differential. TECs function with extremely low pressures (usually high or ultra-high vacuum) to minimise collision of emitted electrons between electrodes, maximising collection and therefore efficiency. The vacuum also provides considerable thermal insulation between the hot emitting cathode and cold collecting anode, allowing the temperature differential to be maintained. Electrons functioning as the work fluid negate the mechanical losses found in conventional methods of power generation, giving TECs huge potential for the future.

$$\eta_{carnot} = 1 - \frac{T_{cold}}{T_{hot}} \quad (4)$$

### 1.2.2 Applications

In the past, cheap and standardised alternatives for power generation relegated thermionic converters to more extreme and niche applications. The onset of the Space Race in the 1960s saw considerable advancements in thermionic technology for non-terrestrial applications. Radioisotopic thermionic converters utilised unstable elements like cerium or actinium isotopes as ‘thermal fuel’.<sup>2</sup> TECs were limited at the time by lack of reliability and challenges in production leading to the adoption of thermoelectric generation (TEG). Thermoelectric generation uses a similar principle of temperature differences creating an electrical potential according to the Seebeck effect.<sup>3</sup> Theoretically it is far less efficient than thermionics due to the diffusive current flow through solid material.<sup>4</sup> Thermionics’ ballistic current flow through a vacuum mitigates this inefficiency. However TEGs were able to generate power at lower temperatures whilst being easier to manufacture. This ultimately led to the adoption of devices like radioisotope thermoelectric generators (RTGs) for space exploration.<sup>5</sup>

Solar power is also a promising area for thermionic application. Photovoltaic cells use photons to produce excitons in a semiconductor. The quantum of energy provided by an individual photon is either above or below the energy of the band gap. The excess energy is lost as heat - thermalization loss; photons with insufficient quanta are not absorbed - absorption loss. Photo Enhanced Thermionic Emission (PETE) uses photon absorption and thermionics in tandem to recoup some of the energy lost through thermalization, improving efficiency.<sup>6</sup> A heterostructured ‘photo’ cathode, bilayered with an absorber and emitter material aids the implementation of the synergistic conversion.<sup>7</sup> Photons excite the electrons to the conduction band of an absorber where they thermalize, giving an equilibrium thermal distribution, the level of which is determined by the temperature of the cathode. Electrons diffuse to the emitter layer and those with sufficient energy to overcome the electron affinity at the surface are ejected.<sup>8</sup> Increasing the efficiency of photovoltaic generation has immediate and growing practical applications.

### 1.2.3 Practical Limitations of TECs

Historically there have been two main limitations to TECs.<sup>9</sup> The first is the interelectrode space charge and the second is the difficulty of finding a suitable high temperature material with a low work function to be used as an emitter.

TECs utilise electrons as their work fluid. In steady operation, the TEC has a positively charged emitter and a negatively charged collector so, once emitted, electrons are attracted back towards the emitter. Thus, electrons with insufficient kinetic energy to reach the collector will be slowed or even fall back towards the emitter and a cloud of electrons will form in the interelectrode gap. This negatively charged space places a further potential barrier for emitted electrons to overcome. Achieving a practical current density requires either a reduction of the space charge barrier or an increase in the kinetic energy of the emitted electrons.

Mitigation of the space charge can be done in two ways. The first is to neutralise the cloud and the second is to prevent its formation. Neutralisation utilises gaseous positively charged metal ions to reduce the potential barrier. Caesium has the lowest electron affinity of any stable element making it the “universal choice” for the vapour.<sup>10</sup> The ions are vaporised from a caesium reservoir within the TEC unit which adds considerable complexity to the unit and decreases its electrical output.

The second route is to reduce the interelectrode gap, decreasing the distance the emitted particles need to travel in the vacuum. The average kinetic energy threshold required to reach the collector is reduced, because the electrons have a shorter distance to travel so fewer electron collisions will occur. Disrupting the cloud by reducing the gap is effective, but at the cost of increasing heat transfer. Near field radiative heat transfer exponentially intensifies thermal energy transfer as the distance between two bodies, in thermal disequilibrium, is decreased past the micron level.<sup>11</sup> This increase in net thermal flux across electrodes makes maintaining a temperature difference problematic and diminishes the efficiency of the unit (Equation 4). The optimal separation for a TEC unit is defined by the wavelength of thermal radiation of the hot emitter ( $\sim 0.9 \mu\text{m}$  to  $3 \mu\text{m}$ ).<sup>12</sup> In practice it is both difficult and expensive to manufacture a device to such a fine tolerance, which has also proved a limitation on their commercial viability.<sup>13</sup>

The electrodes can be biased with a voltage to attract the electrons in the interelectrode gap to the collector, negating the space charge. Whilst this is not viable for power generation it has proven useful for researching emitter materials.<sup>14,15,16,17</sup>

The second practical limitation is to find a temperature stable material with acceptable emitting properties. The material composition is critical but the surface morphology can also substantially alter its thermionic characteristics. Non-planar surface structures can produce local electric fields. This decreases the work function, according to the Schottky barrier lowering of the local area, and electrons emitted in regions with a stronger electric field will accelerate faster than electrons emitted in lower electric fields, amplifying the collected current.<sup>18</sup>

A low work function emitter with surface structures therefore helps reduce the effects of the space charge as well as producing a high thermal conversion efficiency. Nanocrystalline diamond, with its high thermal stability, tuneable electronic properties and multi-faceted micro-structures provides an ideal platform for implementing thermionic technology in the future.

## **1.3 Diamonds**

### **1.3.1 History**

Formed between one and three billion years ago, over 100 miles below the earth's crust, diamonds were first discovered in the alluvium of the Golconda River in India around 2000 BC. Prized for their brilliance and strength, the ancient Greeks believed them to be the tears of gods or splinters from falling stars and called them 'adamas', meaning invincible, this was later translated into Latin as 'diamas'.<sup>19</sup> Diamonds were originally polished and worn as ornaments and talismans to ward off evil, but it wasn't until the 14th century that the art of grinding one diamond into shape by using another and polishing it on a wheel coated with diamond dust was developed.<sup>20</sup> Although known as the hardest natural material, little was understood about the range of its properties until the 20th century.

### **1.3.2 Properties**

Under standard conditions, graphite is the most thermodynamically stable allotrope of carbon. The  $sp^2$  hybridised carbon forms planar layers of hexagonal structures with weak Van der Waals forces holding the sheets together. Delocalised  $\pi$  electrons between the layers allow for conductivity in the plane of the lattice. Diamond is a metastable allotrope of carbon. A tetrahedral arrangement of  $sp^3$  hybridised carbon, with a small atomic radius (0.77 Å), gives the compact structure extraordinary mechanical properties (Table 1). The standard lattice enthalpies of diamond and graphite only differ by 3.9 kJ mol<sup>-1</sup> but a large energy barrier makes diamond extremely kinetically stable.<sup>21</sup>

Table 1: Principle mechanical properties of diamond.

Properties of Diamond	
Hardness (kg / mm <sup>2</sup> )	1.0 × 10 <sup>4</sup>
Density (g / cm <sup>3</sup> )	3.52
Thermal Conductivity (W / cm K)	20.0
Thermal Expansion Coefficient (K <sup>-1</sup> )	1.1 × 10 <sup>-6</sup>
Debye Temperature (K)	2200

### 1.3.3 Synthesis

Diamonds were first made synthetically in the 1950s. The method used, high pressure-high temperature (HPHT), was designed to replicate the conditions of natural formation in the Earth's core. A solvent/catalyst metal was used to lower the energy barrier in a eutectic melt, allowing hydraulic pressure (30,000 – 40,000 atmospheres) and temperature (1,300-1,700 °C) to convert the carbon from sp<sup>2</sup> to sp<sup>3</sup>.<sup>22</sup>

Chemical vapour deposition (CVD) is a method developed in the 1980s and uses a different technique employing an energised hydrocarbon gas mixture to deposit sp<sup>3</sup> hybridised carbon atoms individually onto a template. Low pressure, high temperature hydrocarbons are utilised as the carbon source. Initially graphitic carbon is co-deposited with diamond decreasing yield quality. A gas mixture of hydrogen and hydrocarbon at a ratio of approximately 99:1 is used to give an improved yield. The gas decomposes to give atomic hydrogen which interacts strongly with graphite, etching it off the substrate, but has a negligible effect on diamond.<sup>23</sup>

CVD of diamonds can be effected by either Hot Filament CVD (HFCVD) or Microwave Plasma CVD (MWCVD). The methods are broadly similar: in both the process gases are run through a high temperature chamber at a pressure of approximately 20-100 Torr, decomposing into radical species. A nucleation template is employed to encourage growth - usually in the form of a seeded Mo or Si substrate. The mechanism by which the gaseous radical species deposit diamond onto the template is shown in Figure 2.

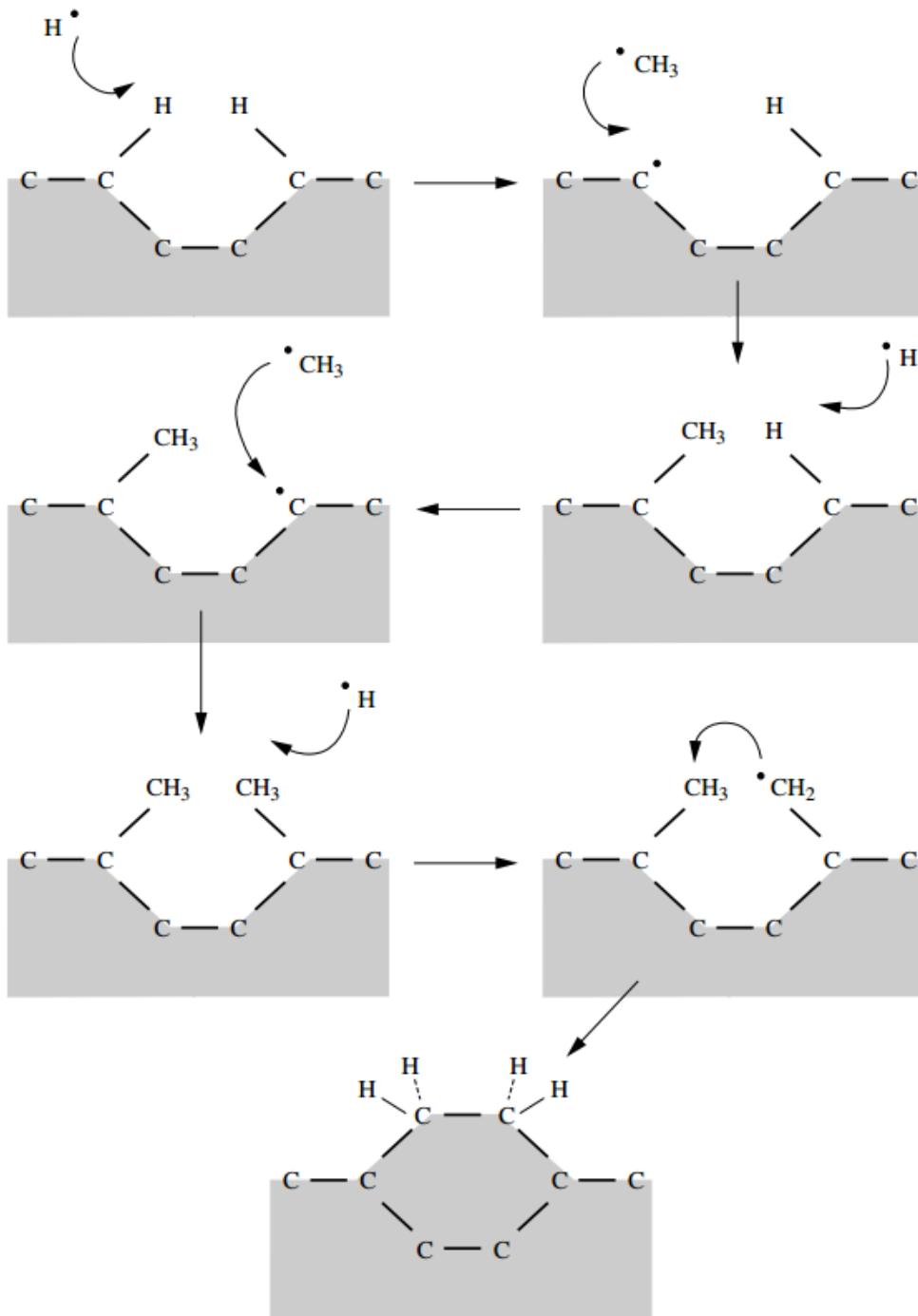


Figure 2: Schematic of stepwise diamond growth using radical hydrogen and hydrocarbon species.<sup>21</sup>

### 1.3.4 Doping

One of the advantages CVD has over HPHT synthesis is that the step-by-step deposition process allows for dopants to be introduced and evenly distributed as the layers are formed.

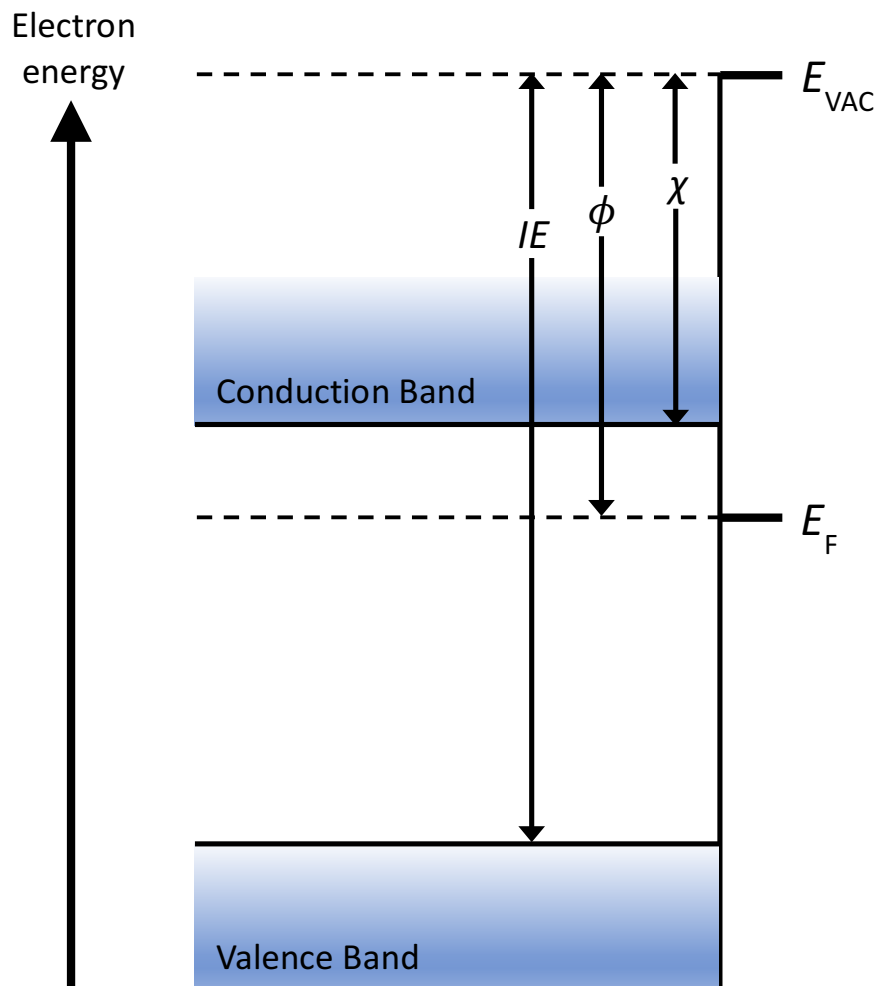


Figure 3: Potential schematic of a semiconductor.  $IE$  represents the ionization energy.

Pure diamond has a wide band gap of 5.45 eV, corresponding to UV wavelength of 225 nm; this makes it both a colourless crystal and an electrical insulator. Lattice defects and impurities alter these properties. For instance naturally occurring coloured diamonds typically exist owing to nitrogen impurities (yellow) and boron (blue). Green diamonds are usually formed due to irradiation and lattice defects cause brown, pink and red discoloration. Doping is used to alter the electronic structure of the bulk material. A semiconductor can be produced by shifting the Fermi level within the diamond band gap (Figure 3).

The Fermi level of a material can be altered by the adding acceptor or donor dopants. Acceptor dopants (p-type) provide electron holes, forming an energy level just above the valence band maximum. Boron is the standard p-type dopant used to improve the conductivity of a diamond. It has a similar covalent radius to carbon (0.88 Å compared to 0.77 Å) allowing direct substitution into the carbon lattice. Boron is trivalent, and so can only bond with three of the neighbouring four  $sp^3$  hybridised carbons, producing an ‘electron hole’. These holes can reduce the Fermi level to 0.37 eV above the valence band.<sup>24</sup>

Donor dopants (n-type) have an additional electron, which is left weakly attached to the dopant atom in the lattice. This electron maintains an energy level just below the conduction band minimum, and so can be promoted easily. Nitrogen provides the closest covalent radius to carbon for an n-type dopant at 0.74 Å. Substitutional incorporation of nitrogen leads to a deep donor level in diamond of 1.7 eV below the conduction band.<sup>25</sup> Shallow donor levels can be produced by changing the dopant to phosphorus (0.6 eV) or even co-doping with silicon (0.09 eV).<sup>26,27</sup>

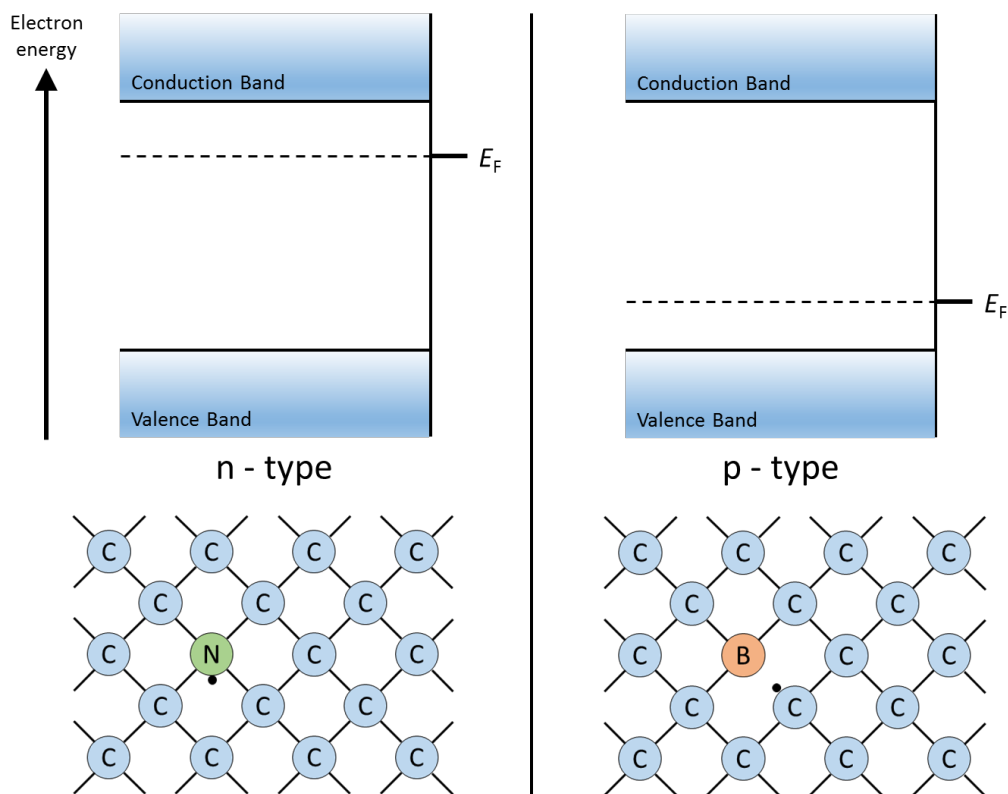


Figure 4: Schematic of n-type (nitrogen) and p-type (boron) doped semiconductor showing the different positions of the dopant induced Fermi levels.

Surface atoms possess unsatisfied atomic bonds that modify the charge distribution of the dopants. This produces a non-uniform density of states (e.g.  $\pi$  type surface states) with respect to the bulk, creating band bending.<sup>28</sup> Dopant positioning, concentration and charge determine the extent and type of the bending.<sup>29</sup> The band potential increases towards the surface for n-type dopants producing an upward band bend, whilst p-type doping give a downward shift in the band (Figure 5).

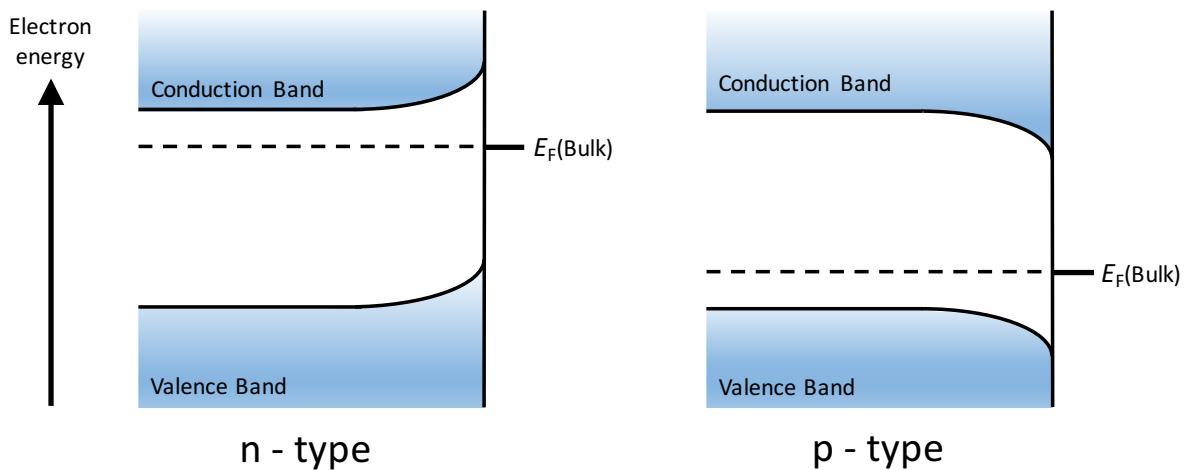


Figure 5: Illustration of the surface effects of n-type and p-type dopants on the potential profile.

### 1.3.5 Surface Morphology & Termination

Diamond surfaces consist of three primary planes: [100], [110] and [111] (Figure 6).<sup>30</sup> Each crystal plane has different surface properties. [111] and [110] have one dangling  $sp^3$  bond per surface atom, whereas [100] has two. In order to stabilise the lone electron of the dangling bond the surface undergoes reconstruction, termination or both.

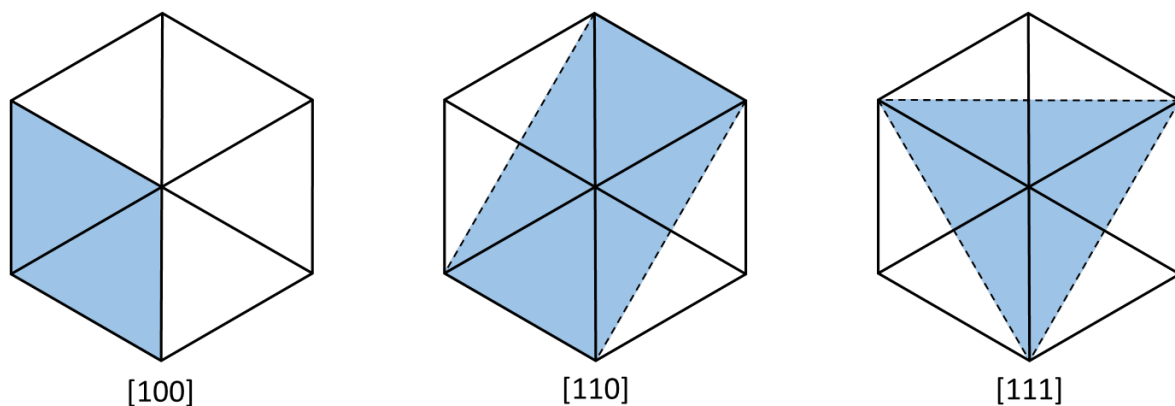


Figure 6: Representation of the primary planes.

Surface reconstruction converts two  $sp^3$  surface carbons to form a  $\pi$  bonded  $sp^2$  system (i.e. (100)-(2 × 1)). Termination is the chemisorption of a range of different species like hydrocarbons, oxygen or hydrogen onto the surface atoms to lower the energy of the  $sp^3$  hybridisation (i.e. (110)-(1 × 1):H).<sup>31</sup>

Since free electron density is approximately 5 orders of magnitude lower in semiconductors than it is in conductors ( $\sim 10^{17} \text{ cm}^{-3}$  compared to  $\sim 10^{22} \text{ cm}^{-3}$ ) the ability of semiconductors to screen electric fields is lowered, allowing penetration in the order of  $\sim 100 \text{ \AA}$  into the bulk. This allows the electric field from surface dipoles to penetrate the diamond creating a space charge region, inducing band-bending.

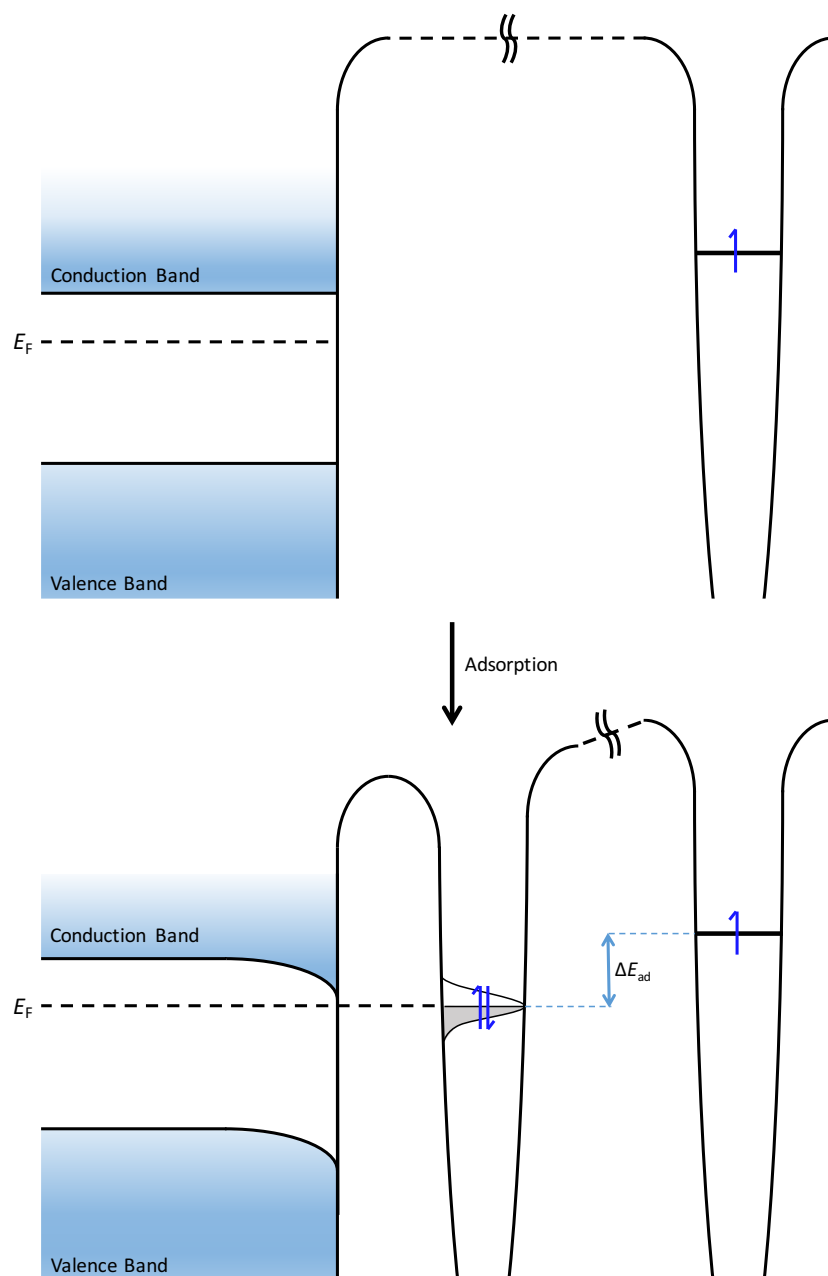


Figure 7: Schematic showing the energy level diagram of a hydrogen atom and an n-type semiconductor without interaction (A) and an adsorbed hydrogen atom on the surface of an n-type semiconductor with a non-interacting hydrogen atom for comparison (B). Dopant induced band bending has been omitted for clarity. Adapted from Z. Zhang *et al.*<sup>32</sup>

Figure 7 shows how the adsorption of hydrogen onto the surface effects the potential profile of both the semiconductor and the hydrogen. The lone electron of the unsatisfied surface atom pairs with the electron in the half-filled hydrogen orbital. The molecular orbital formed is broadened due to Heisenberg's uncertainty principle. The energy of the orbital is lowered ( $\Delta E_{ad}$ ) via transfer of electron density to the bulk, allowing the broadened orbital to find equilibrium with the Fermi level of the bulk. The charge transfer between the semiconductor and the hydrogen atom induces a surface dipole producing downward band bending.

The atomic Fermi level is the theoretical basis of electronegativity.<sup>33</sup> Surface terminations will induce dipoles whenever there is a difference in electronegativity between the terminating agent and the bulk. Figure 8 shows how the direction of the band bending produced is dependent on the orientation of the surface dipole.

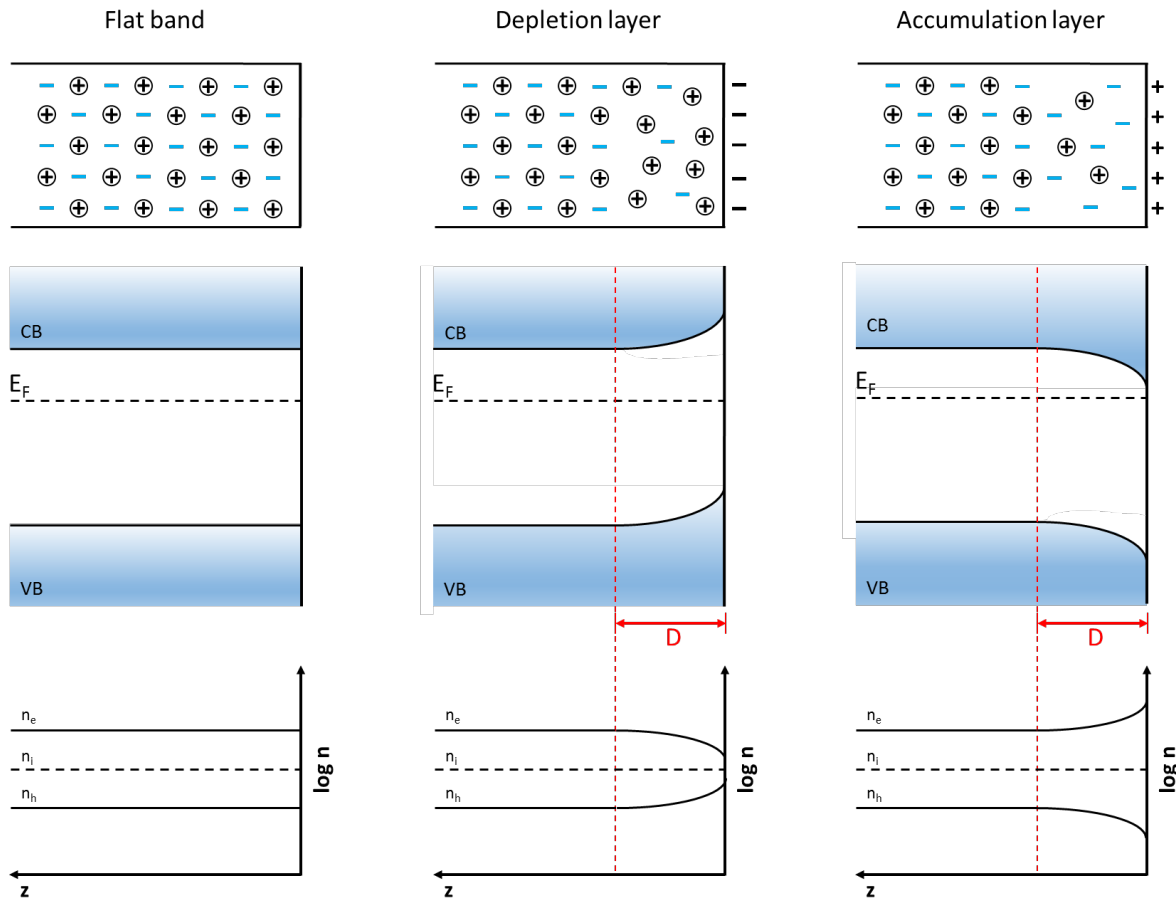


Figure 8: Schematic diagrams showing the energy level diagram and free charge carrier densities for an n-type semiconductor. The charge region, D, marks the penetration depth of the field.  $n_e$  = free electron;  $n_h$  = free hole density;  $n_i$  = intrinsic carrier density. Dopant induced band bending has been omitted for clarity.

Hydrogen is common terminating agent for CVD diamond and has a significantly lower electronegativity than carbon (2.2 versus 2.55). This creates a dipole that promotes an accumulation layer within the charge region. The termination induced band bending can combine constructively or destructively with the dopant induced band bending and amalgamating these effects can produce significant variations in the electron affinity. A destructive combination is shown in Figure 9 as the dopant and termination induced band bending counteract each other.

### Nitrogen-doped, $N_D=10^{20} \text{ cm}^{-3}$

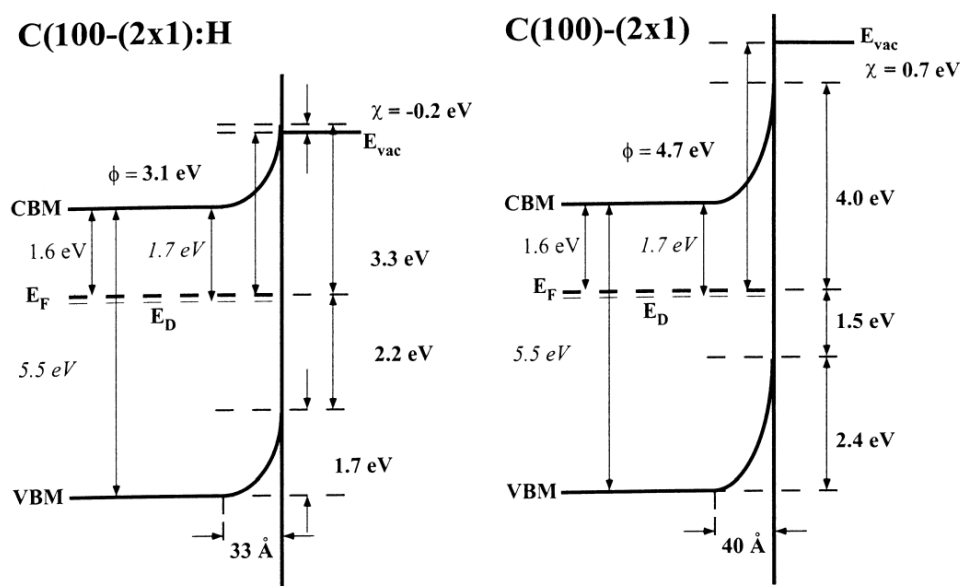


Figure 9: The effect of hydrogen termination on Nitrogen doped CVD C(100) diamond.<sup>34</sup>

Figure 9 shows how a negative electron affinity (NEA) is formed when diamond is terminated with hydrogen, as well as the flattening of the upward band bend. NEA occurs when energy of the conduction band minimum is higher than  $E_{vac}$ .<sup>35</sup> This means that electrons in the conduction band at the surface of the diamond are higher in energy than those in vacuum.

The formation of a NEA surface can be seen across all the primary planes with hydrogen adsorption (Table 2). The instability of the hydrogen termination is dependent on the surface and termination type. The monohydrogenated surface will desorb at elevated temperatures.<sup>36</sup> The dihydrogenated surface (100)-(1 × 1):2H is highly unstable due to steric interactions and will reconstruct to give a (2 × 1):H geometry at very low temperatures.<sup>37</sup>

Table 2: Electron affinity values for different planes of diamond.

Diamond Surface	$\chi$ (eV)
(100)-(2 × 1)	0.8 <sup>38</sup>
	0.75 <sup>39</sup>
(100)-(1 × 1):2H	-3.4 <sup>38</sup>
(100)-(2 × 1):H	-1.3 <sup>40</sup>
	-1.0 <sup>41</sup>
	-2.2 <sup>38</sup>
(110)-(1 × 1)	0.6 <sup>39</sup>
(110)-(1 × 1):H	-1.0 <sup>41</sup>
(111)-(2 × 1)	0.5 <sup>39</sup>
(111)-(1 × 1):H	-1.07 <sup>42</sup>
	-0.9 <sup>41</sup>

## 1.4 Beta Enhanced Thermionic Emission (BETE)

The theories outlined in the previous sections have led to substantial improvements in thermionics. BETE is a novel concept which is intended to take this a step further. There are three ways beta radiation can potentially enhance thermionic emission:

### 1. Perturbation of the space charge:

High energy beta particles interact with the low energy electrons in the interelectrode gap. This disrupts the space charge and thereby reduces the average energy needed for the emitted electrons to reach the collector. This would increase collected current density.

### 2. Secondary emission (SE):

High energy betas particles interact with the surface electrons, increasing their energy. A small minority of these electrons will escape the surface creating secondary emission.<sup>43, 44</sup> This would increase emitted current density.

### 3. Radiation-Induced Conductivity (RIC):

High energy betas particles interact with the valence electrons of the emitter promoting them into the conduction band, generating electron-hole pairs (EHPs). This would increase the number of free charge carriers in the material, which in turn would enhance conductivity and act as a multiplier for emission.

Diamond is ideally suited as a candidate BETE material. High thermal conductivity, low thermal expansion and an ability as a semiconductor when doped provide the necessary base properties. Additionally, it has a compact lattice giving a high electron density which increases the chance of beta interaction. Its low atomic number gives minimal electron backscattering and bremsstrahlung radiation. This gives an efficient transfer of energy from the incident betas to the emitter material, making diamond an ideal candidate for beta enhancement.

## 2 Experimental

### 2.1 Overview

The aim of the experiments was to determine to what degree beta radiation enhances thermionic emission. In order to do this in a controlled and repeatable environment existing TEC equipment was modified to incorporate a  $^{63}\text{Ni}$  beta source and a  $^{59}\text{Ni}$  control. Fourteen NCD emitters, termed ARMo 1 - 14, were fabricated under identical conditions.

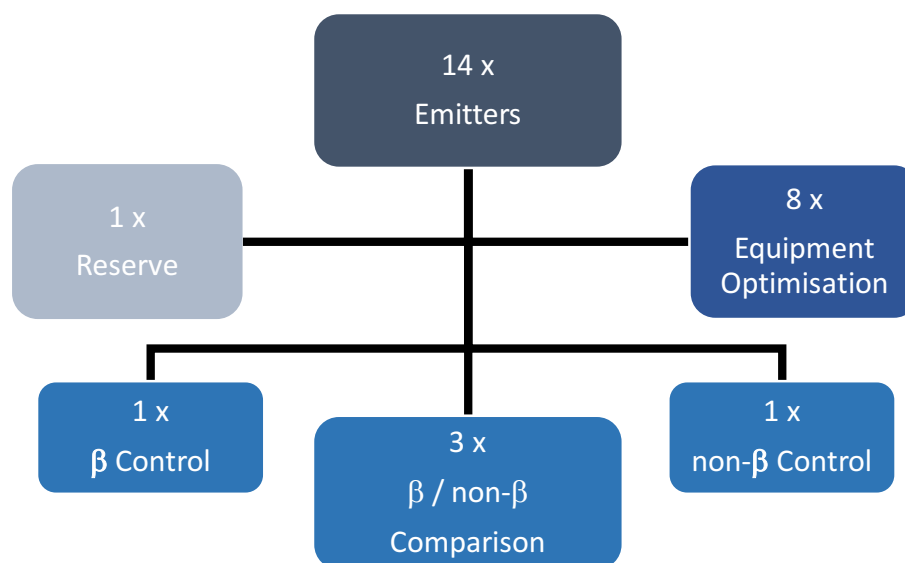


Figure 10: Schematic of the emitter usage.

Figure 10 shows how the samples were used over the course of the project. Initially eight emitters were used to ensure the modified TEC equipment was functioning consistently within acceptable parameters. Out of the remaining six emitters, five were used to test for beta enhancement (2 as controls and 3 as comparators) and one was held in reserve.

### 2.2 Equipment

#### 2.2.1 Emitter

The nitrogen doped nano crystalline diamond (NDNCD) films were grown on molybdenum substrates. Each had a surface area of  $1\text{cm}^2$  and a thickness of  $500\ \mu\text{m}$ . Nitrogen incorporation, high grain boundary density and  $\text{sp}^2$ -bonded graphitic carbon are believed to enhance thermionic emission because the defects caused directly contribute electronic states within the diamond band gap.<sup>45, 46</sup> The emitters were hydrogen terminated to reduce the work function and improve emission. Hydrogen terminated NDNCD has a reported emission value which ranges from  $0.84$  to  $70\ \text{A cm}^{-2}\ \text{K}^{-2}$  and has a low reported work function of around  $2\ \text{eV}$ .<sup>47, 48, 49</sup> Molybdenum was used due to its high melting point, high thermal conductivity,

strong carbide and acceptably low coefficient of thermal expansion. The molybdenum was seeded by submerging the substrates first in a carboxyethylsilanetriol di-sodium solution (25 %, Fluorochem) and then a suspension of sonicated 18 nm diamond (25 cts/kg, Microdiamond) to aid nucleation.

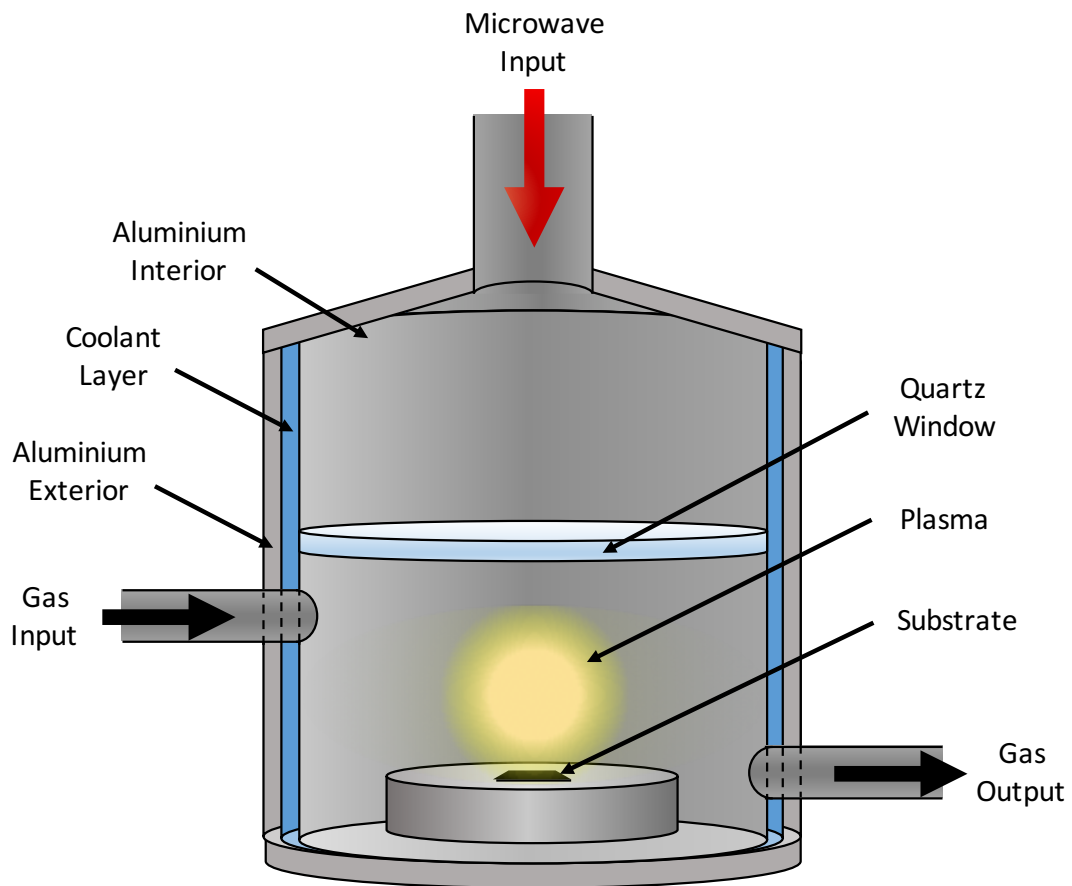


Figure 11: Schematic of the MWCVD reactor.

Figure 11 depicts the core of MWCVD reactor used to grow the NDNCD. The plasma was created using 2.45 GHz microwave radiation generated by a 1.5 kW ASTeX Magnetron. The quartz window allows radiation to penetrate the vacuum chamber and produce a plasma. The microwave input was tuned to minimise reflected watts and prevent damage to the generator. The chamber used an internal water jacket as coolant system with a Raytek Thermalert SX optical pyrometer measuring substrate temperature (not shown).

The NDNCD film was grown over a period of precisely 15 minutes with both a power to pressure and a methane to nitrogen ratio of 10:1 (Table 3). This relatively short period of the growth yielded a NCD layer under a micron thick.<sup>50</sup>

Table 3: Microwave plasma reactor conditions used in NCD growth.

Diamond growth	
Time (min)	15
Pressure (Torr)	130
Power (Watts)	1300
Hydrogen flow (sccm)	300
Methane flow (sccm)	12.6
Nitrogen flow (sccm)	1.26

Molybdenum is a refractory metal and therefore is a poor emitter and absorber of radiation. This makes it difficult to radiatively heat but equally reduces IR heat loss. To increase the efficiency of heat absorption a refractory plasmonic grating was employed and a polarised CO<sub>2</sub> laser ( $\lambda = 10.2 - 10.8 \mu\text{m}$ ) was then used to heat the back of the emitter. The molybdenum was laser scribed with a  $10.6 \mu\text{m}$  grating (Figure 12), creating surface microstructures similar in size to the wavelength of the incident photons. This satisfies the conditions for surface plasmon polariton excitation and improves the efficiency of radiative heating.<sup>51</sup>

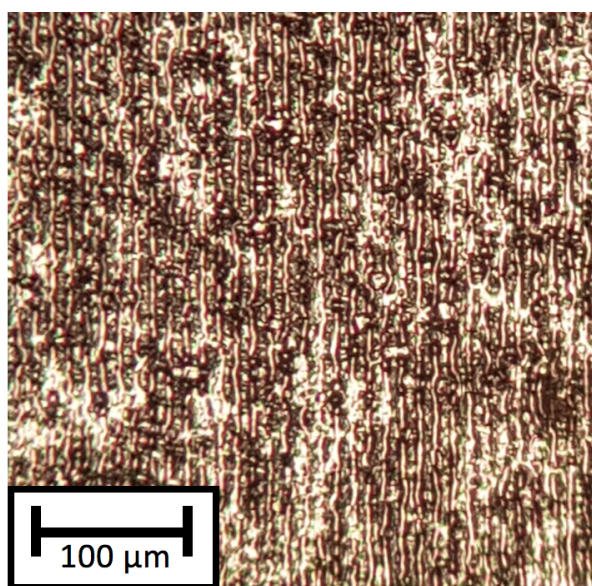


Figure 12: Molybdenum surface with a  $10.6 \mu\text{m}$  laser scribed grating.

The hydrogen termination was achieved by bathing the diamond surface in a pure hydrogen plasma in a two-step system as outlined in Table 4. The first (cleaning) phase used a high-energy plasma to strip the surface of any contaminants and the second (terminating) phase used a low-energy plasma to fill the surface sites with hydrogen.

Table 4: Microwave plasma reactor conditions used in hydrogen termination.

Hydrogen termination	
Step 1 - Cleaning phase	
Time (min)	2
Pressure (Torr)	85
Power (Watts)	1200
Hydrogen flow (sccm)	300
Step 2 - Terminating phase	
Time (min)	2
Pressure (Torr)	30
Power (Watts)	700
Hydrogen flow (sccm)	300

Each sample was analysed using Raman spectroscopy to confirm that all the NCNCD films were of similar composition. Measurements were taken with Renishaw 2000 Laser Raman Spectrometer with an excitation wavelength of 514 nm. Figure 13 shows the spectrum for the 5 emitters used to investigate for beta enhancement, ARMo 9-13, and the emitter held in reserve, ARMo 14.

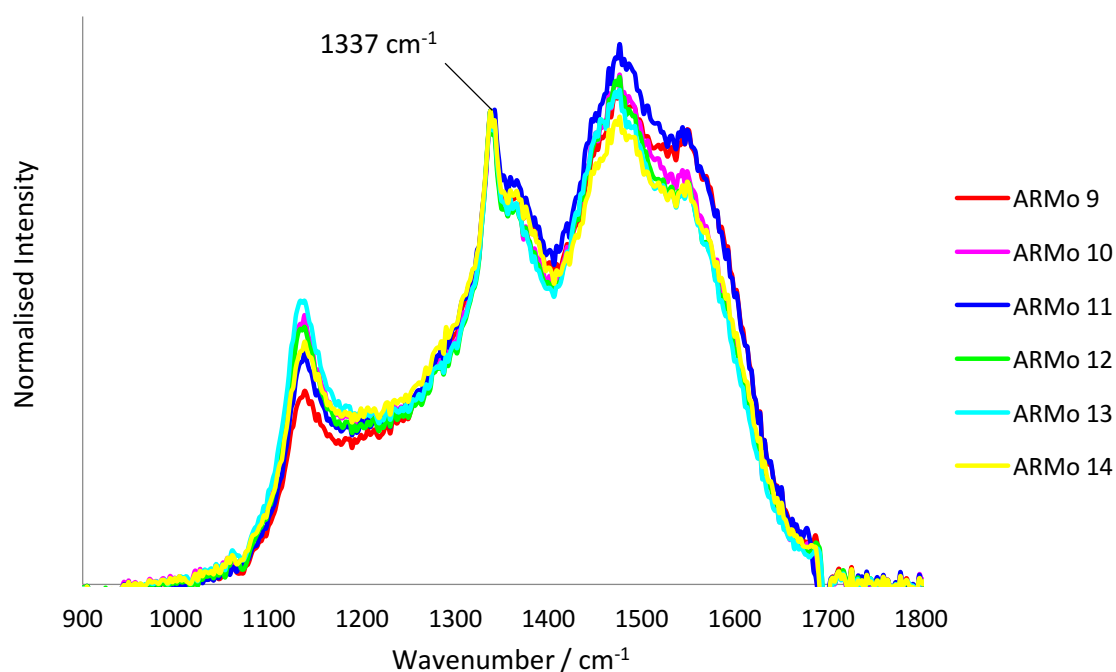


Figure 13: The Raman spectrum with the intensity normalized to the 1337  $\text{cm}^{-1}$  peak.

The Raman spectrum confirmed the presence of nanocrystalline diamond (1337  $\text{cm}^{-1}$  peak). The diamond is present in a much greater proportion than the spectra would initially suggest as green light excitation is approximately 50 times more sensitive to  $\text{sp}^2$  carbon ( $\pi$ -bonded amorphous carbon and graphite (1544  $\text{cm}^{-1}$ )) than to the  $\text{sp}^3$  carbon.<sup>52</sup> The peaks at 1140  $\text{cm}^{-1}$  and 1470  $\text{cm}^{-1}$  are attributed to *trans*-polyacetylene in the films grain-boundaries and are an accepted indicator of NCD.<sup>53</sup>

Additionally, scanning electron microscopy (SEM) was used to confirm the sub-micron crystal size (Figure 14). The image, taken with Zeiss Sigma HD Field Emission SEM, also shows the multifaceted surface with heterogeneous morphology which is characteristic of NCD films.

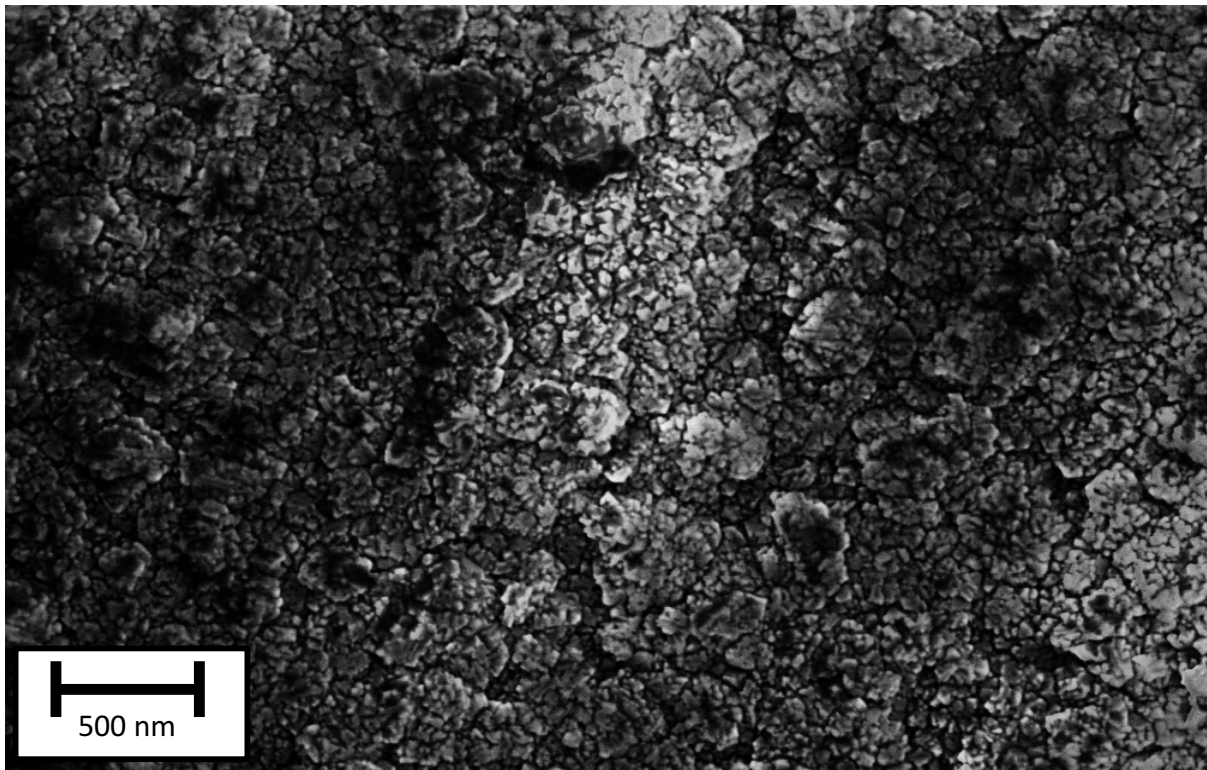


Figure 14: Nanocrystalline surface of ARMo 14.

### 2.2.2 Collector

$\text{Ni}^{63}$  was used as the beta source. To attempt an even distribution of  $\beta$  particles the source had to be integrated into either the collector or the emitter because the small interelectrode gap made lateral irradiation difficult to achieve. The collector was chosen to incorporate the source in order to avoid the exposure of radioactive material to high energy plasmas. The original steel collector was modified with a molybdenum adapter to hold a  $3 \times 3$  mm  $100 \mu\text{m}$  foil of either  $^{63}\text{Ni}$  (2.6 MBq) or  $^{59}\text{Ni}$  (0 MBq) (Figure 15).

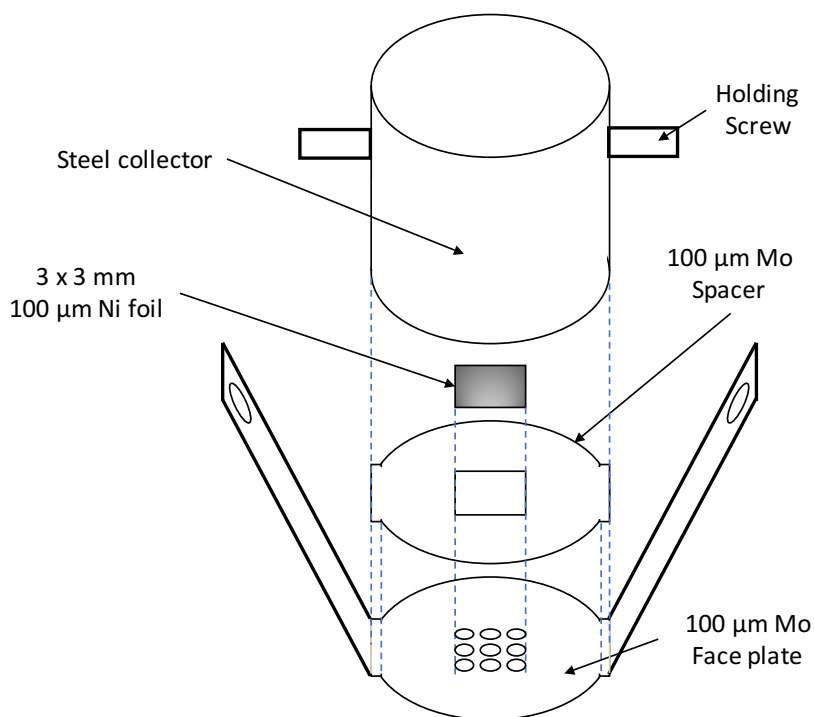


Figure 15: Schematic of the molybdenum adapter.

The holes in the face plate exposed 50.3% of the Ni foil, allowing approximately half the high energy  $\beta$ 's to interact with emitter (Table 5).

Table 5: Radioactive properties of  $^{63}\text{Ni}$

Radioisotope $^{63}\text{Ni}$	
$\tau_{1/2}$ (annum)	100.1
$\beta$ Radiopurity (%)	>99
$E_{\beta(\text{avg})}$ (keV)	17.5
$E_{\beta(\text{max})}$ (keV)	70.0

### 2.2.3 TEC

The emitter was held under vacuum and radiatively heated by a polarized Synrad Firestar 40 Watt  $\text{CO}_2$  laser with a Land SPOT R160 optical pyrometer monitoring the temperature. A proportional–integral–derivative (PID) controller was used to control the energy input *via* a feedback loop between the laser and the pyrometer.

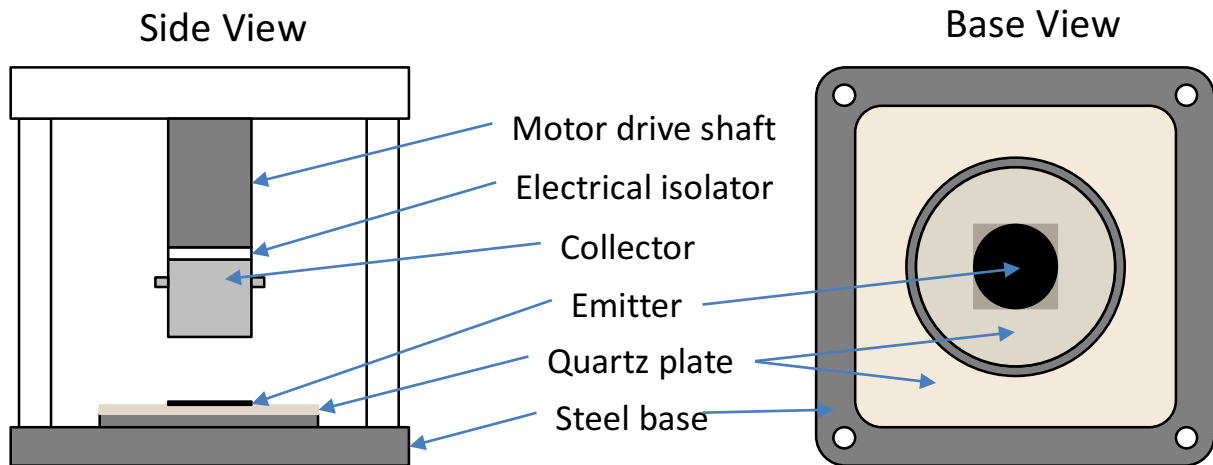


Figure 16: Diagram of the TEC core (wiring and clamps have been omitted for clarity).

Quartz was used to hold the emitter because of its thermal and electrical insulation properties. The interelectrode gap was controlled by a piezo-electric motor to ensure a constant spacing. The TEC core (Figure 16) was then suspended in a vacuum chamber as outlined in Figure 17.

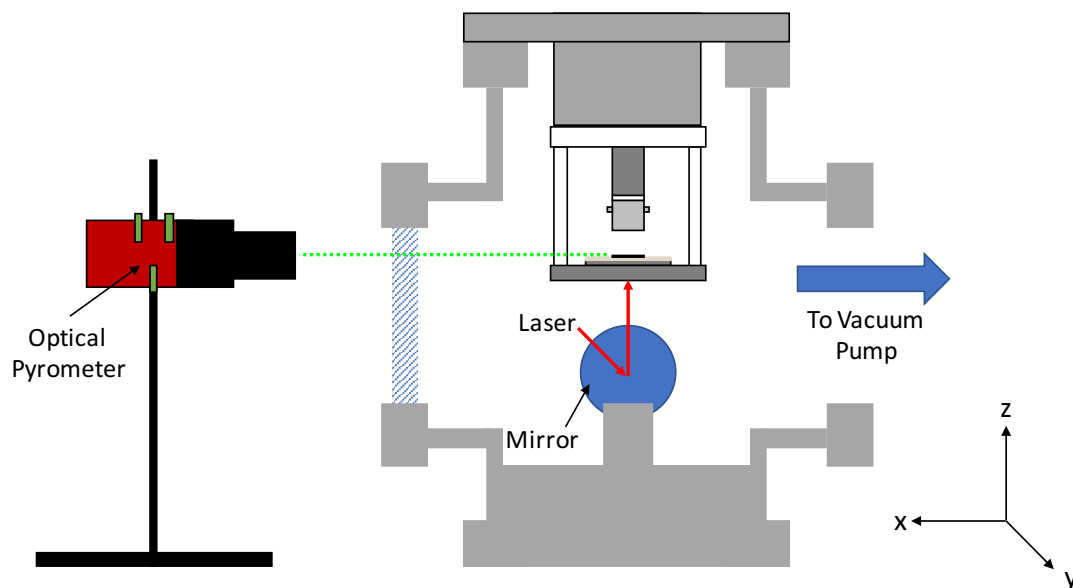


Figure 17: Schematic of the original TEC set up with free standing pyrometer. The laser beam enters along the y axis and is reflected up onto the emitter base.

The initial TEC set up used a thermocouple in thermal contact with the diamond surface of the emitter. This allowed the pyrometer (which has a minimum operating temperature of 240 °C) to be calibrated against the side of the emitter. However, the thermal contact was not consistent so the TEC was modified. A mirror was installed to allow the base (instead of the side) to be measured. Since the base had a larger surface area emitting black-body radiation, the temperature measurements were less susceptible to error (Figure 18). The pyrometer was permanently secured to the chamber removing the need to recalibrate for each experiment.

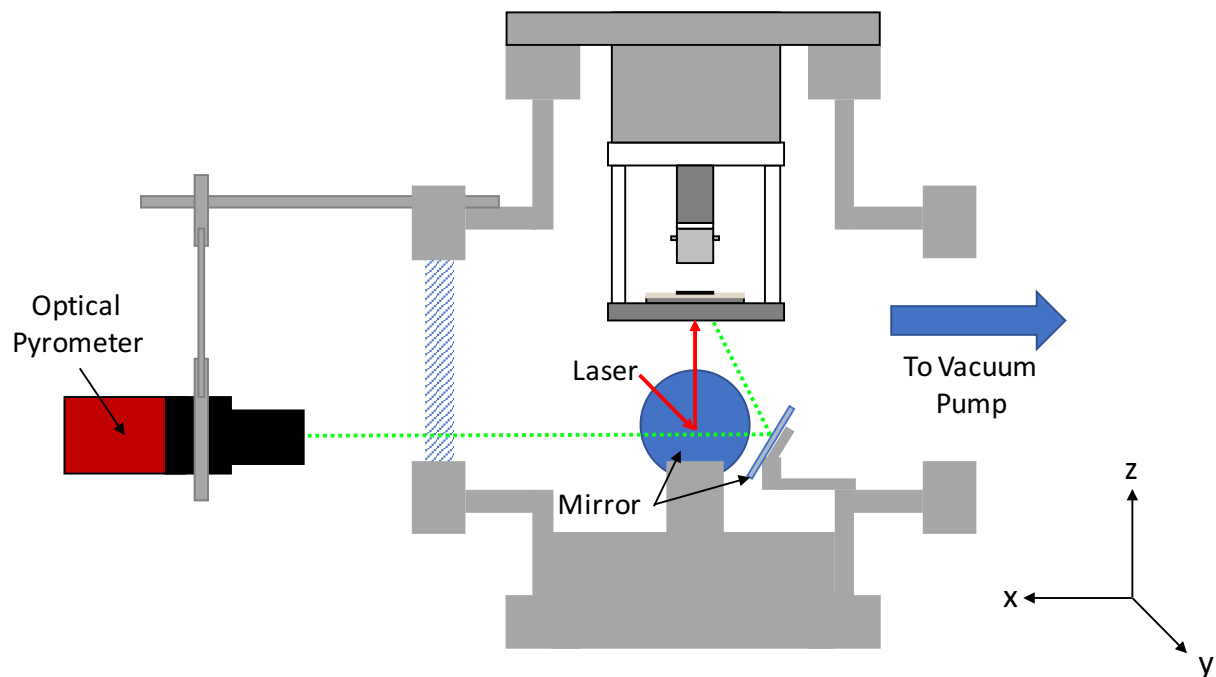


Figure 18: Schematic of the upgraded TEC set up.

## 2.3 Methodology

### 2.3.1 Profile

The temperature profile was adjusted to cycle the emitter between 300 and 600 °C. This range was chosen because the NCDs emission threshold was established at between 400 and 500 °C, using the first eight emitters. The pyrometer readings were cross checked against a type-K thermocouple, secured to the diamond surface to ensure good thermal contact. This confirmed the temperature profile was consistent.

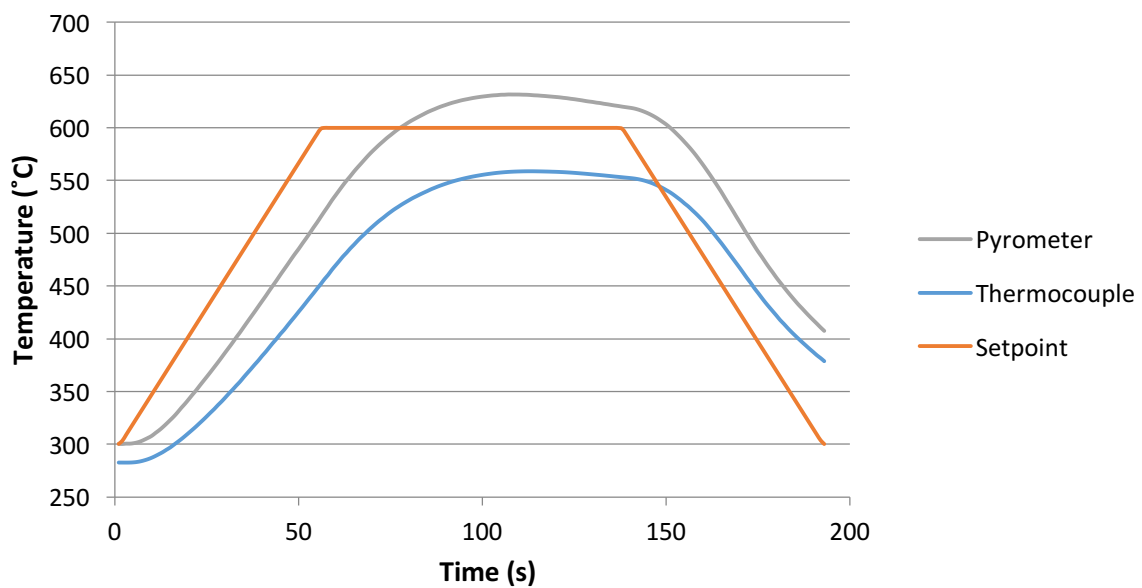


Figure 19: The set point temperature profile with the pyrometer and thermocouple readings averaged over 20 profiles. Pyrometer  $\sigma_{\bar{x}} = 0.36$  °C, Thermocouple  $\sigma_{\bar{x}} = 0.64$  °C.

The feedback loop overshoot the 600 °C set point on the pyrometer consistently in each profile. The thermocouple confirmed the diamond surface had a similar, albeit cooler, temperature profile. The true emitter temperature is assumed to be within the boundaries of the thermocouple and pyrometer in Figure 19.

### 2.3.2 Run

In order to observe the effect of the termination on beta enhancement, the terminated sample was put through 20 consecutive temperature profiles, with 60 seconds' rest at 300 °C between each profile. The unstable hydrogen termination desorbs at elevated temperatures. This process, termed a "Run", allowed the effects of this desorption to be analysed (Table 6).

Table 6: Conditions used for measurement Runs.

Measurement Run	
Number of profiles	20
Bias (V)	25
Interelectrode Gap (µm)	200
Pressure (Torr)	$< 5 \times 10^{-6}$

The 5 samples (ARMo 9 – 13) were used to test BETE and each was put through 4 Runs giving a total of 400 individual profiles. ARMo 10, 11, 13 were used to evaluate BETE with ARMo 9 and 12 acting as controls for beta and non-beta respectively (Table 7). Each emitter was hydrogen terminated prior to every Run.

Table 7: Experimental design to test for beta enhancement.

		ARMo				
		9	10	11	12	13
Run	1	β	β	x	x	β
	2	β	x	β	x	x
	3	β	β	x	x	β
	4	β	x	β	x	x

## 3 Results

### 3.1 Thermionic Emission

#### 3.1.1 Emission Profile

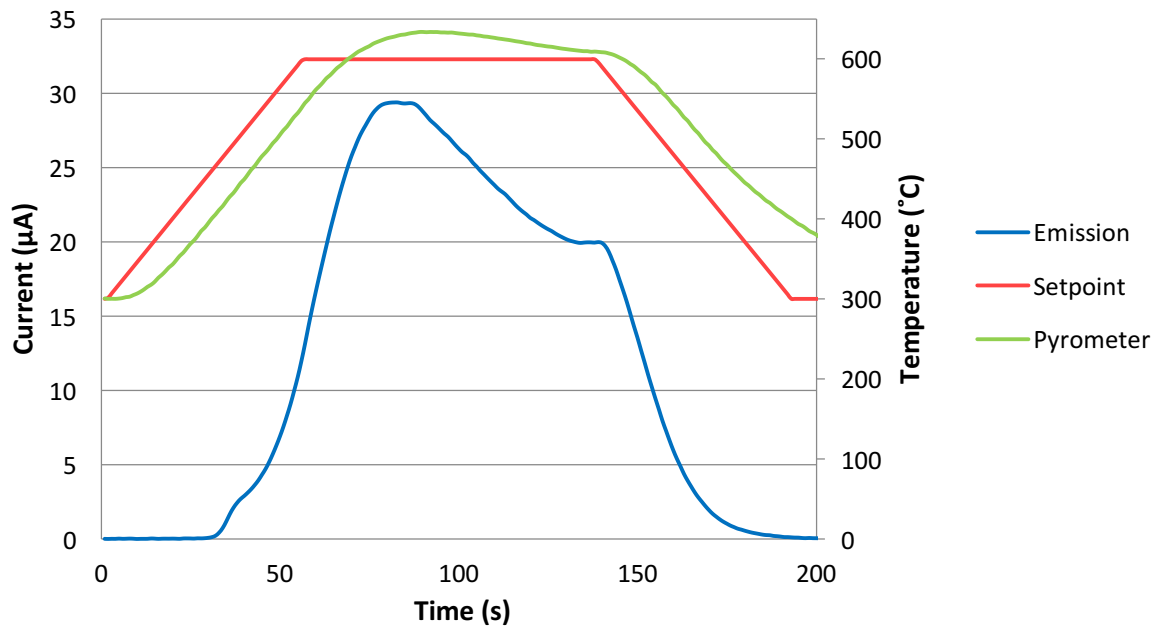


Figure 20: A standard emission profile with emission current on the primary y-axis and temperature on the secondary y-axis. Data taken from the 5<sup>th</sup> profile of the 3<sup>rd</sup> Run of ARMo 12 (<sup>59</sup>Ni).

Figure 20 depicts the typical thermionic behaviour of the emitters over the temperature profile. The emission is seen to be highly temperature dependant. Once the temperature exceeds the emission threshold ( $\sim 420$  °C in this case) the current increases rapidly with temperature. Further a 3 % drop in temperature from (628 °C to 608 °C) causes a 31 % decrease in current from its peak at 29  $\mu$ A to 20  $\mu$ A. This fall of 20 °C, between 90 and 145 seconds, was caused by the feedback loop correcting the overshoot.

This current drop is further exaggerated by the desorption of the termination. The rate of desorption is greater at higher temperatures which damages the low function properties of the emitter, decreasing emission. The instability of the hydrogen surface can be seen in Figure 20 as the emission peaks 5 °C before the temperature maximum. The profile is broadly comparable to the Richardson-Dushman model for thermionic emission as shown in Figure 21.

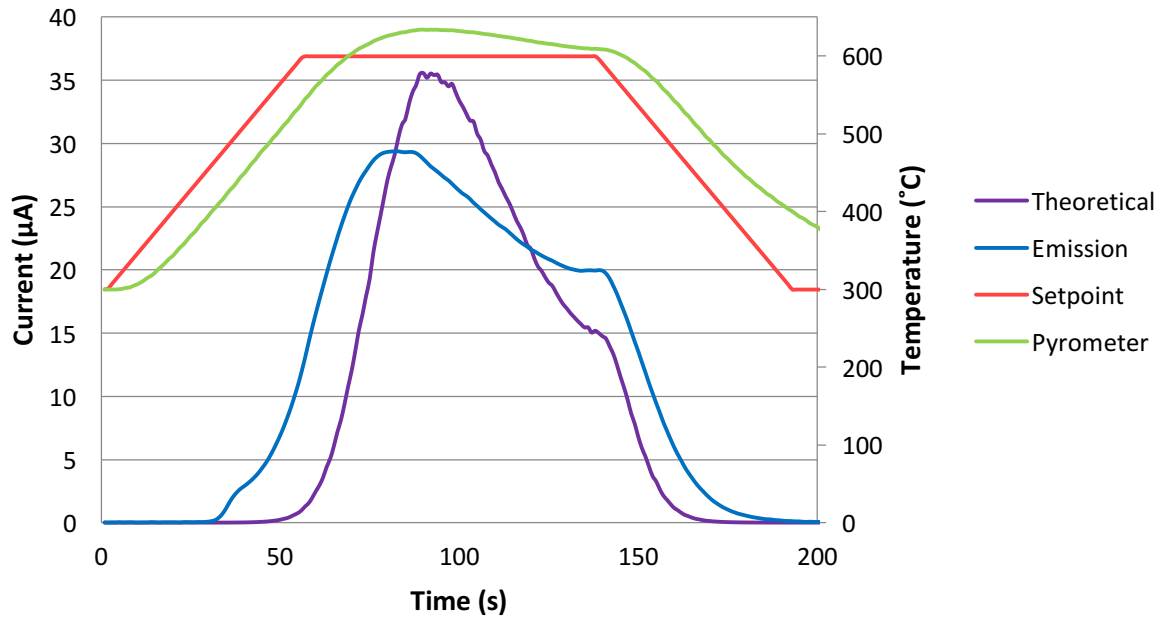


Figure 21: The Richardson-Dushman equation was used to model the theoretical current. Data taken from the 5<sup>th</sup> profile of the 3<sup>rd</sup> Run of ARMo 12 (<sup>59</sup>Ni).

In Figure 21 the theoretical current was modelled using the Richardson-Dushmann equation. The ideal Richardson constant along with the current and temperature from the peak of emission was used to determine the work function of the emitter. The work function was then inputted into the equation and used to extrapolate the theoretical current over the temperature profile. As can be seen from Figure 21 the Richardson-Dushman model produces a reasonable approximation of the actual emission. However, there are three major flaws with the model:

1. The modifier for the Richardson constant is unknown for the emitter so the ideal constant was used.
2. The NDNCD film has multiple crystals with varying facets giving multiple sites with differing work functions. The actual current is the sum of the individual emissions from all these sites.
3. The model makes no specific allowance for the termination desorption.

### 3.1.2 Emission Run

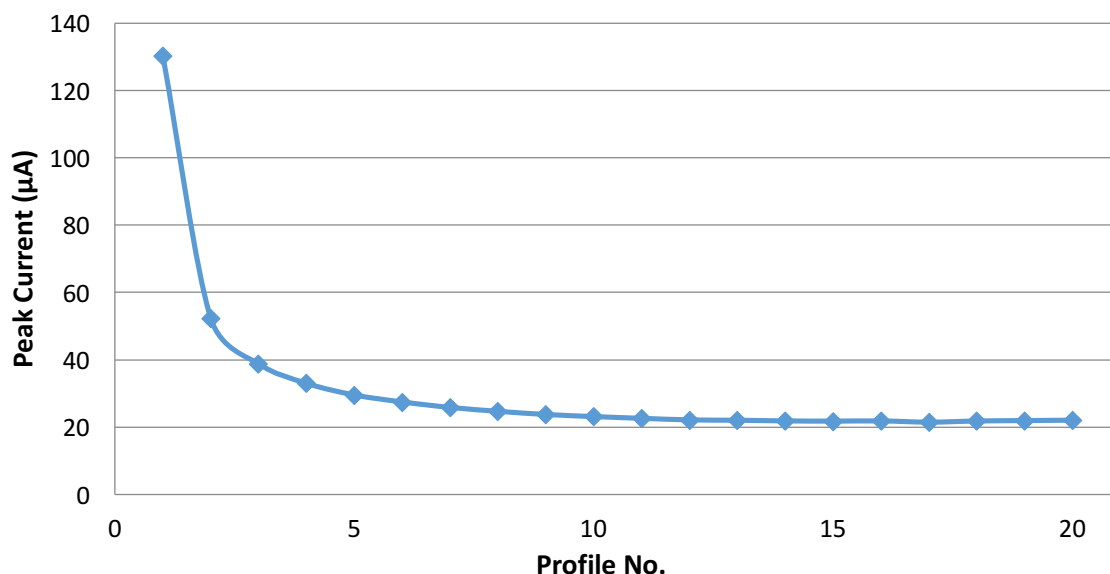


Figure 22: The peak emission from every profile over the Run. Data taken from the 3<sup>rd</sup> Run of ARMo 12 (<sup>59</sup>Ni).

Each Run constituted 20 profiles. Figure 22 compares the peak emission of each profile. The instability of the termination is evident. The decrease in emission can be seen to mirror the first order isothermal desorption of the hydrogen termination. Different environments on the surface produce varying termination bond strengths. The sites with longer C – H bonds are weaker and have lower thermal stability. The initial rapid decline (Profile 1 to 2) in peak emission is due to the destruction of the most unstable sites.

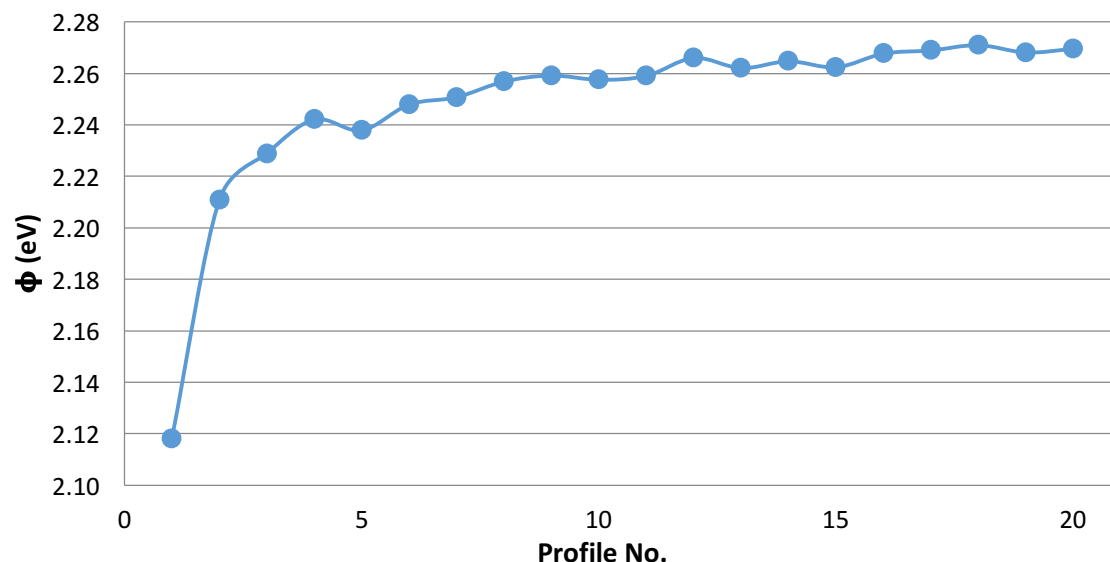


Figure 23: The effective work function of the emitter calculated from the Richardson-Dushman equation using the peak emission and corresponding temperature for in each profile. Data taken from the 3<sup>rd</sup> Run of ARMo 12 (<sup>59</sup>Ni).

As the emitter has multiple sites with different work functions, the Richardson-Dushman model, when applied to the  $1 \text{ cm}^3$  sample, produces an “effective” work function which is a rough summation of the work function from every site. For the Richardson-Dushman equation to produce the results in Figure 22 the effective work function would have to be varied between 2.12 and 2.27 eV (Figure 23) because desorption raises the barrier to emission.

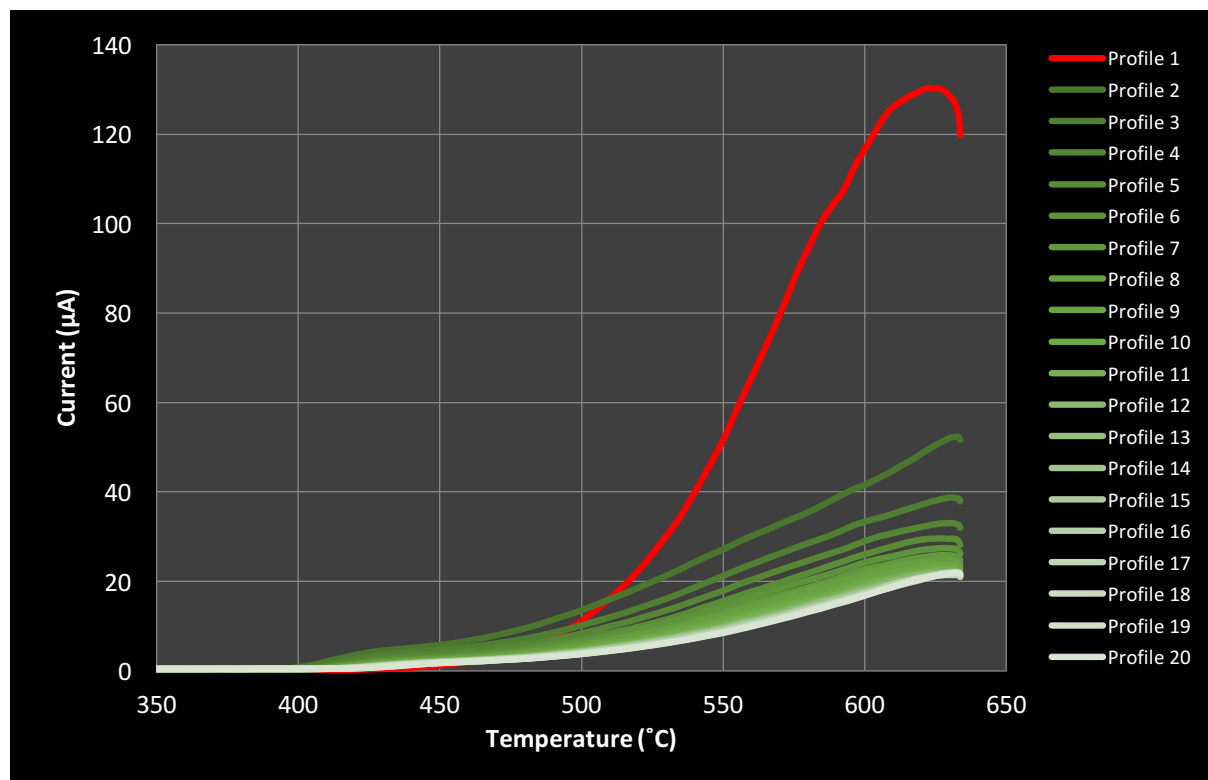


Figure 24: The emission current against temperature for the heating section of each profile. Data taken from the 3rd Run of ARMo 12.

Figure 24 shows the emission across the thermal range with each sequential profile. Profile 1 shows has the highest gradient above the emission threshold. This is because the sites with the lowest work function produce the highest emissions, but are also less stable and so the first to desorb.<sup>54</sup> This largely accounts for the difference in gradient between the first and subsequent profiles, although resistive heating of the highest emission sites could also play a factor in termination degradation. The slight downward slope at the right hand side of every profile, as the maximum temperature is reached, also demonstrates this effect. Figure 25 graphs the hysteresis cycle of the initial profile and the  $50 \text{ }\mu\text{A}$  drop at  $600 \text{ }^\circ\text{C}$  between the heating and the cooling phase, further attesting to this degradation.

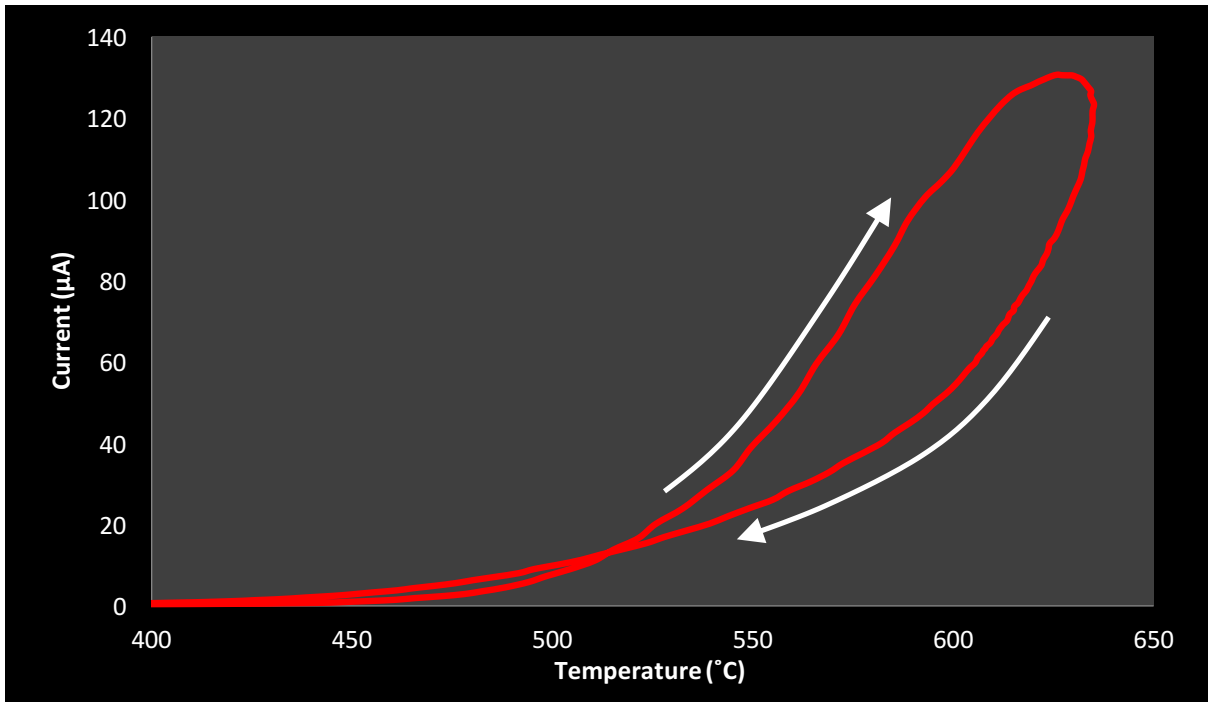


Figure 25: Hysteresis cycle for the first profile of the Run. Data taken from the 3rd Run of ARMo 12.

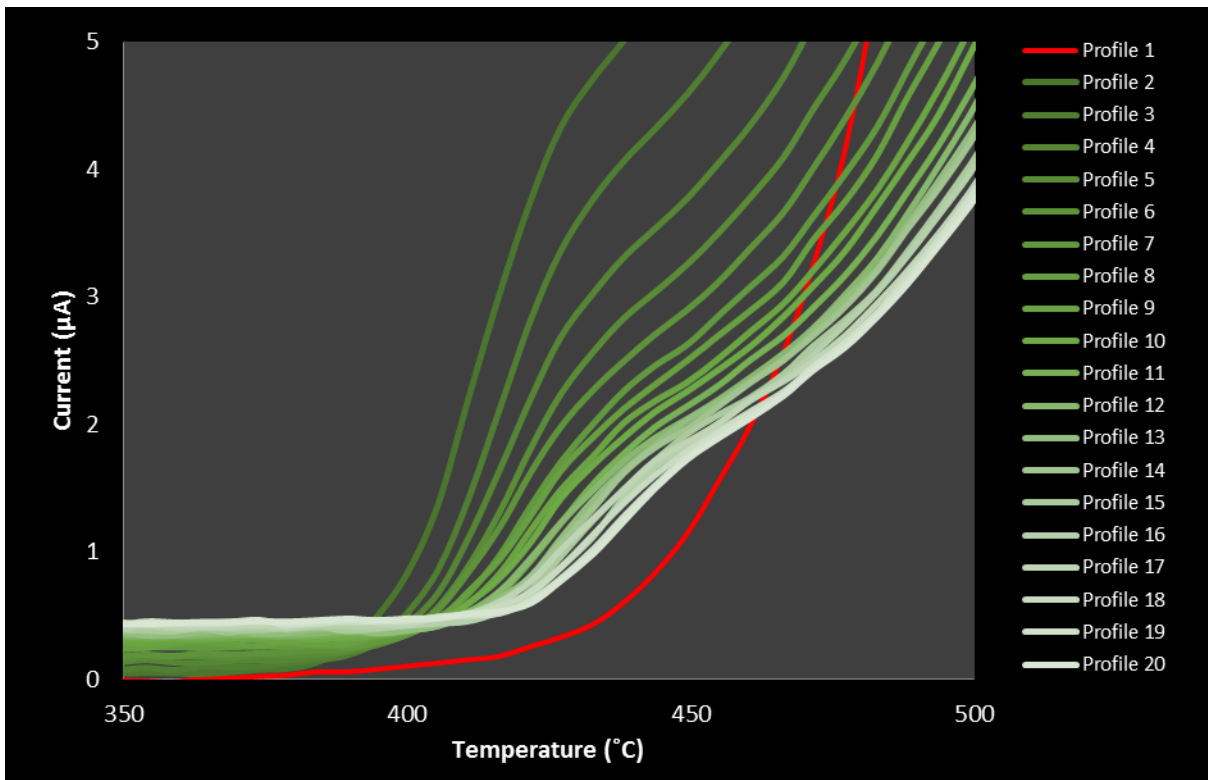


Figure 26: The emission threshold. Data taken from the 3rd Run of ARMo 12.

Figure 26 focuses on the initial emission and shows that, with the exception of the first profile the temperature threshold increases for each profile over the Run. The first profile, is distinctive due to the desorption of atmospheric surface contaminants such as hydrocarbons and sodium, lowering the effective work function of the emitter at the very start of the Run.

The emission threshold is determined by the lowest work function sites that produce measurable emission. The destruction of these sites over the subsequent profiles causes the temperature threshold to be raised by over 25 °C from the 2<sup>nd</sup> to the 20<sup>th</sup> profile.

The emission threshold for the Run is defined as the temperature at which 1 μA of emission occurs on the 2<sup>nd</sup> profile - in this instance it is 405 °C. The Richardson-Dushman equation gives the emission threshold occurring at  $k_B T > \phi$ . The rise in the temperature threshold is in agreement with Figure 23 that the effective work function increases over the course of the Run.

## 3.2 Beta Enhanced Thermionic Emission

### 3.2.1 Overview

To ensure that successive Runs produced data which was within acceptable error limits four Runs from both the  $\beta$  and non- $\beta$  control were performed sequentially (Figure 27). In spite of the identical growth conditions each emitter will have unique defects and morphology so the data from each sample should only be compared with other data from the same sample. Emission data was averaged over 4 Runs for each emitter and gave consistent results. Figure 27 shows the error bars for the controls, derived from the standard error of the mean. The relatively small error between Runs is likely to be due to the regeneration of the hydrogen surface. Whilst this is thought to have no significant effect on surface morphology, some alterations such as etching are probable due to the nature of the high-energy plasma.<sup>55</sup>

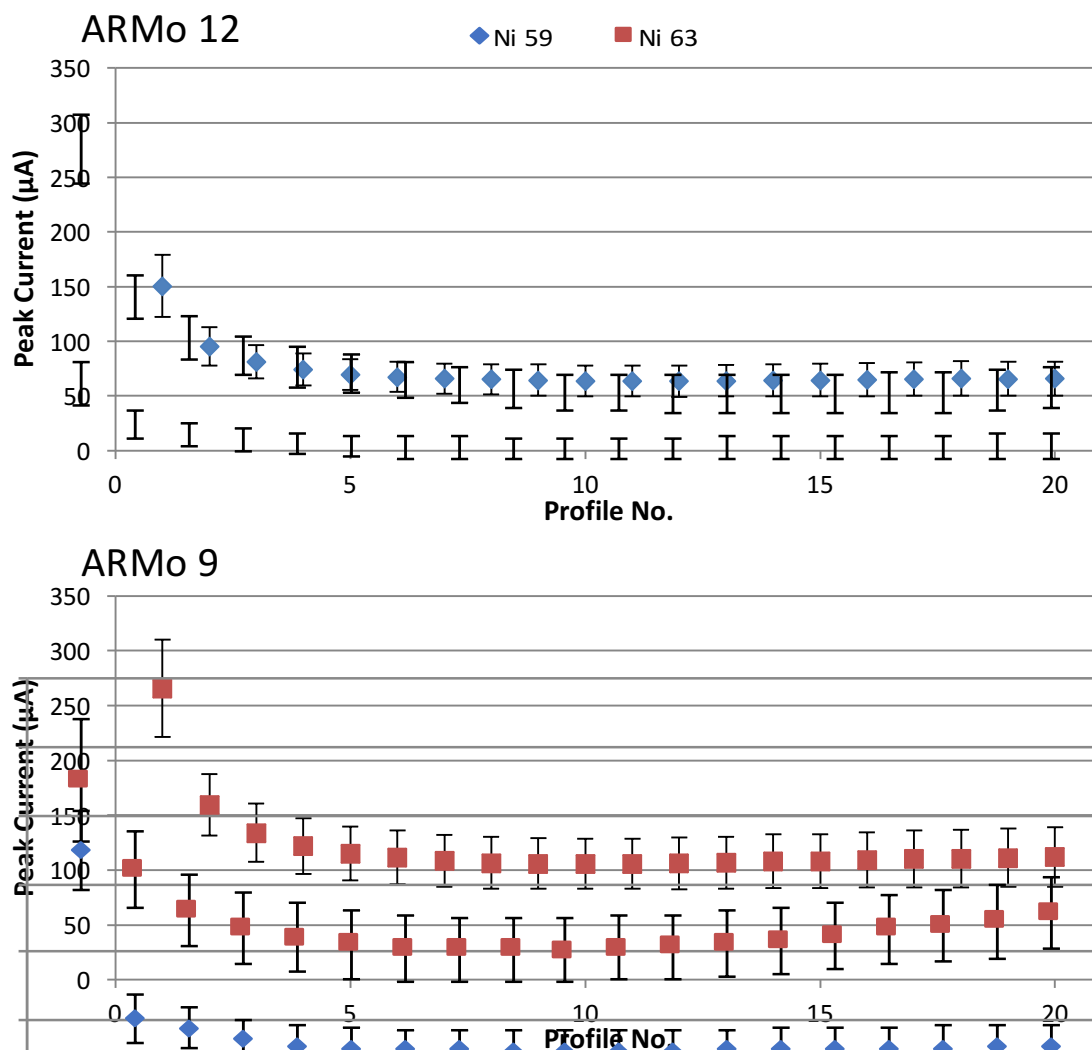


Figure 27: The average of  $\beta$  and non- $\beta$  controls. Error bars were derived from the standard error of the mean of the four Runs.

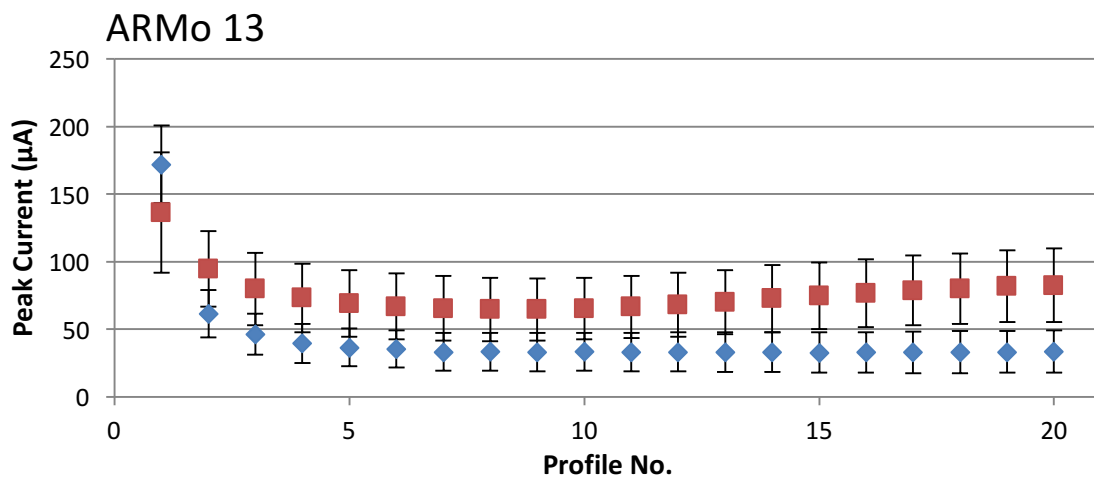
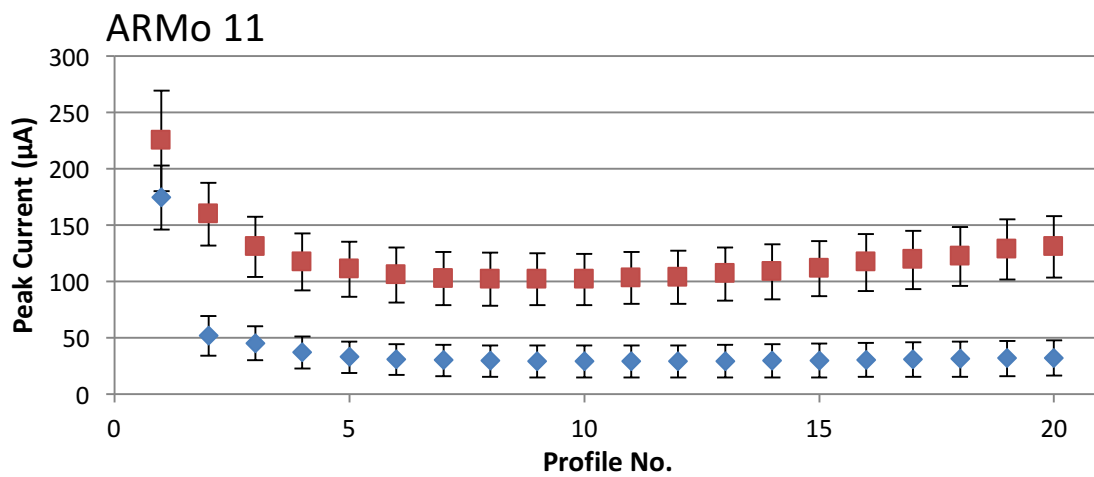
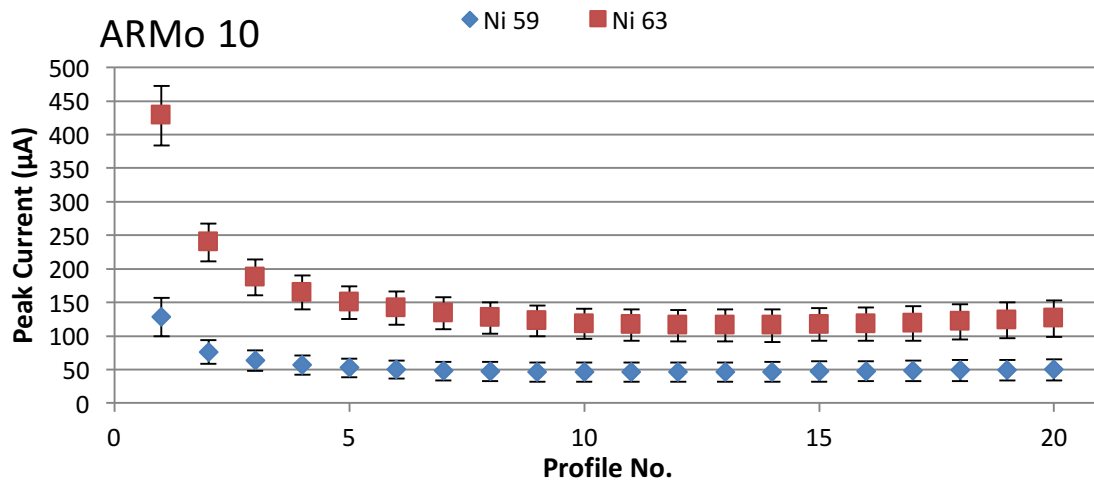


Figure 28: The average peak current of the two  $\beta$  and non- $\beta$  Runs for each comparative sample. The error bars were extrapolated from the controls.

Figure 28 shows that in every case beta radiation significantly augmented the current generation of the emitter. Figure 29 takes the average of all the comparative Runs. The 2.3 MBq source induced an average emission increase in excess of 100%.

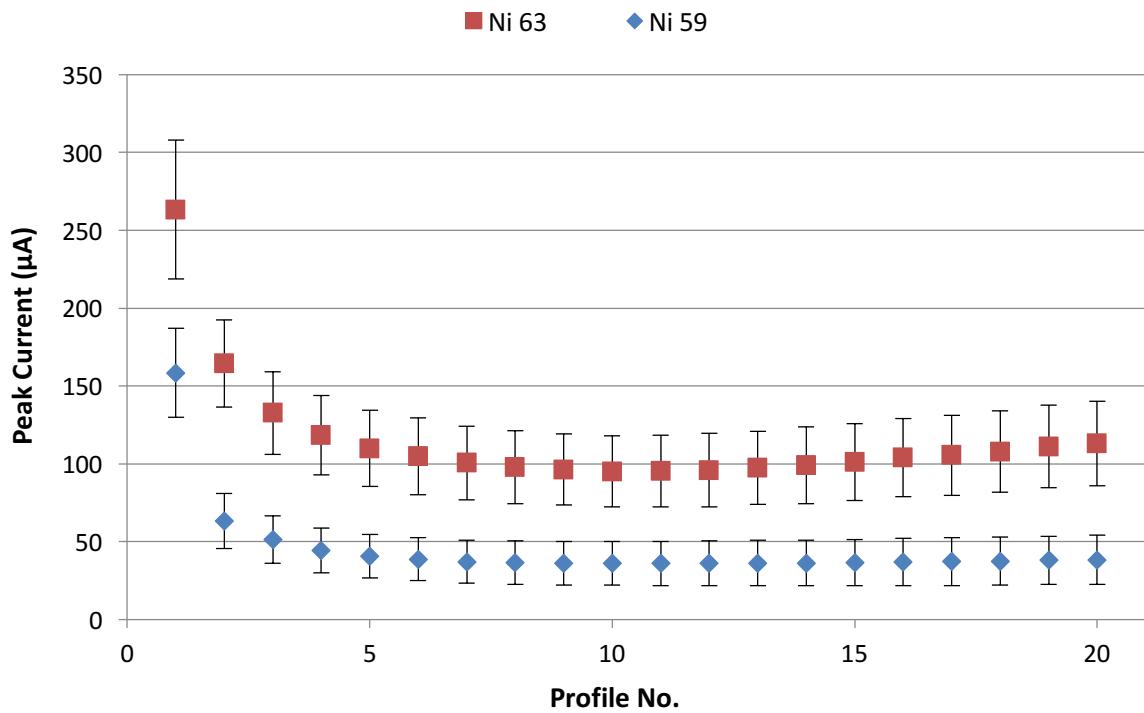


Figure 29: Overall comparison of the average of the peak currents of six  $\beta$  and non- $\beta$  Runs across three samples.

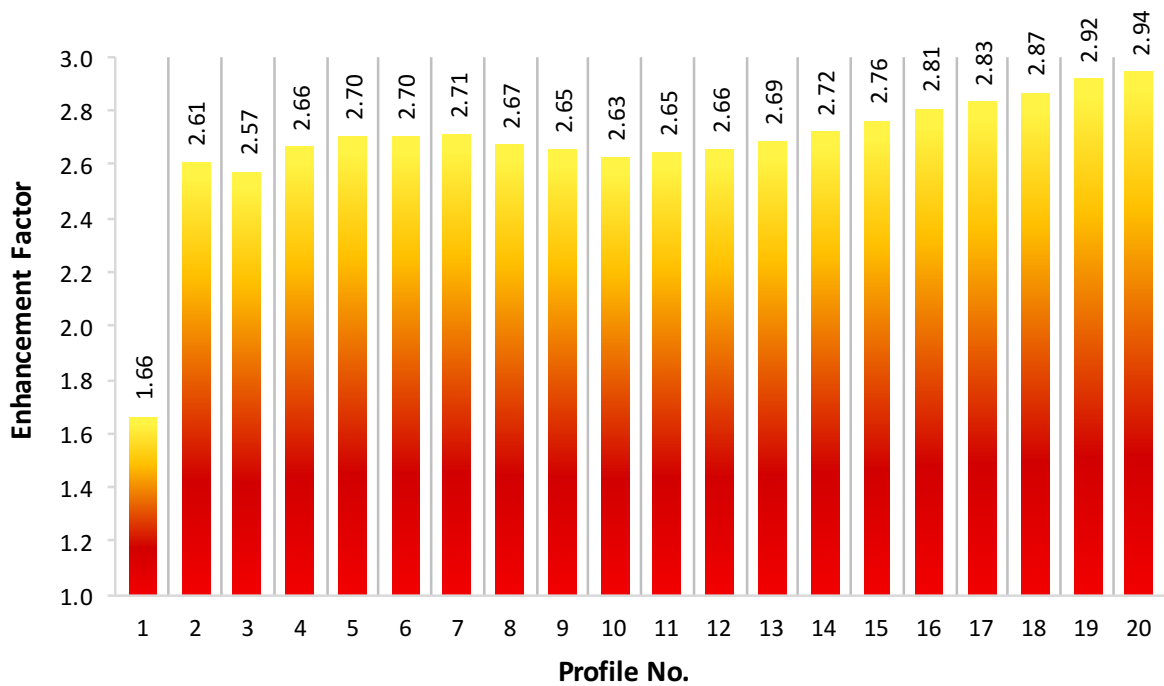


Figure 30: The average emission enhancement for the six  $\beta$  and non- $\beta$  seen as a multiplier for each profile over the course of the Run.

Figure 30 gives an average enhancement factor of 2.72 between the second and 20<sup>th</sup> profiles. The first profile is an outlier due to the highly volatile nature of the initial termination causing the peak emission to occur at a lower temperature (Figure 31). Its result, therefore, can be seen as anomalous.

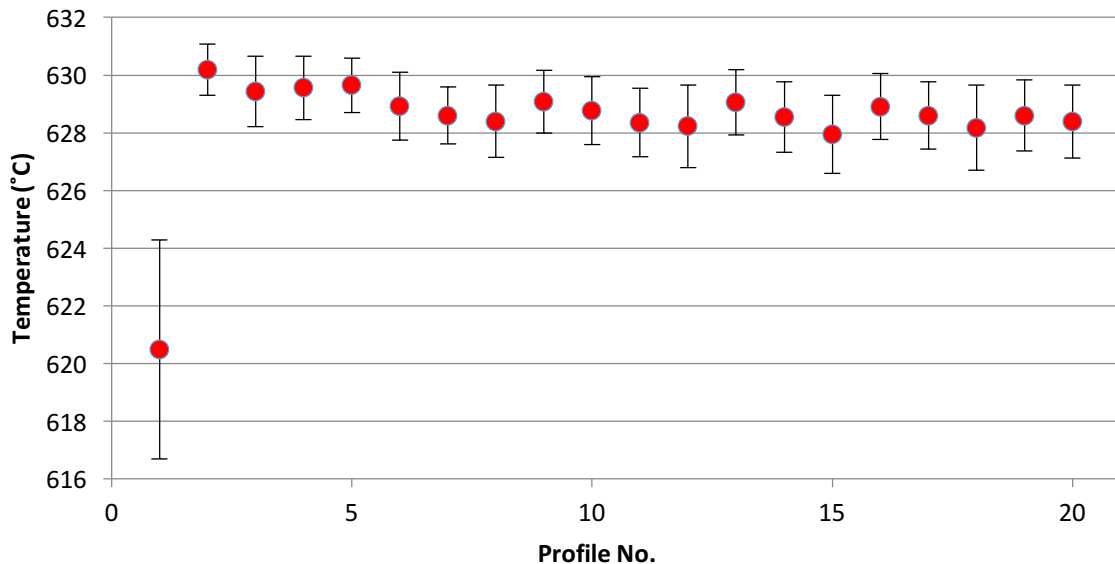


Figure 31: Average pyrometer reading for the peak emission of each profile for all Runs on ARMo 9-13.

### 3.2.2 Hypotheses

Below is a consideration of each of the posited causes of beta enhanced thermionic emission and the evidence to support it:

#### 1. Perturbation of the space charge:

The space charge perturbation was not measured in this experiment as it was Run in transmission mode with a 25 V bias. The experiment was conducted in TEC mode (0 V bias) with the <sup>63</sup>Ni source and no emission was collected. This lends credence to disproving the theory of space charge perturbation but is not conclusive evidence as no emission was collected with <sup>59</sup>Ni either.

#### 2. Secondary Emission:

Secondary emission does occur but does not adequately account for the increase seen. Assuming an maximum yield in transmission mode of 200 secondaries for every incident  $\beta$ , the 2.6 MBq source with 50 % exposure would produce an additional 42  $\mu$ A, 6 orders of magnitude lower than the actual enhancement attained.

### 3. Radiation-Induced Conductivity (RIC):

Electron-hole pair (EHP) generation in the bulk increasing the quantity of free charge carriers in the n-type semiconductor is currently the only viable theory to explain the beta phenomenon. Increased conductivity within the bulk of the emitter enhances thermionic emission by allowing a greater proportion of excited electrons to reach the surface and so increase the ballistic electron flow across the interelectrode gap.

$$\phi_{EHP} = \frac{E_{\beta}}{2.5 \times E_g} \quad (5)$$

Equation 5 provides an approximate explanation for this effect. It states the yield is determined by the energy of the incident particle,  $E_{\beta}$ , and the energy of the band gap,  $E_g$ .<sup>56</sup> Applying Equation 5 a 17.5 keV beta particle could produce over 1500 EHPs in a diamond medium. The electron cascade generated along the path of the primary particle as it travels from the surface to the bulk creates channels with high conductivity for thermally excited electrons to reach the vacuum interface, producing a gain in emission.

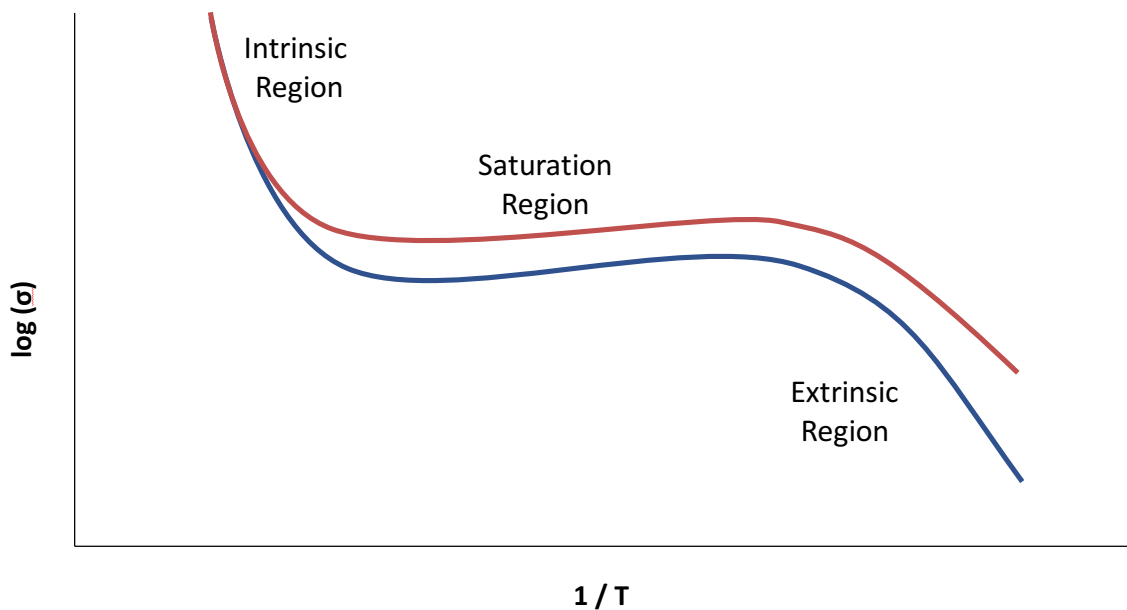


Figure 32: Schematic of the log of conductivity against the inverse temperature for a semiconductor (blue) and an irradiated semiconductor (red).

Figure 32 demonstrates the potential effect of RIC. At low temperatures there will be few ionized deep donors in an n-type semiconductor. As the temperature increases more donors ionize, increasing the number of free charge carriers. The saturation region is reached when all the donors are ionized. However, increased lattice scattering at higher temperatures reduces the mean free path of the electron and reduces conductivity. The excitation provided by beta irradiation increases the number of free charge carriers across the temperature range. Thermionic emission is most effective as the temperature approaches the saturation region as, with diamond, the material will degrade in the intrinsic region.

### 3.3 Emission Threshold

The threshold temperature has little correlation to the peak emission (Figure 33). The sites responsible for the initial emission will contribute to the peak emission but, due to higher desorption rates and a low density in comparison to the rest of the active sites at the temperature maximum, they have little influence.

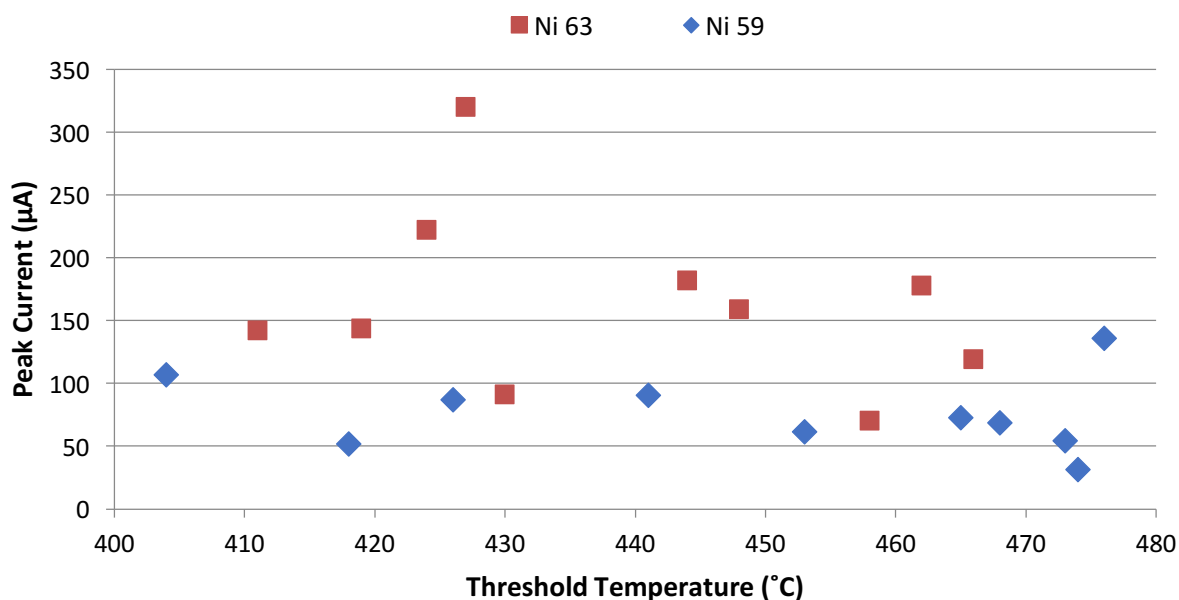


Figure 33: Emission threshold for the 2nd profile against the peak emission for the 2nd profile for all Runs on ARMo 9-13.

Figure 34 shows that the average emission threshold for every emitter decreases with each consecutive Run. This indicates an increase in the density of the low work function sites from termination regeneration, though this does not appear to alter the peak emission levels.

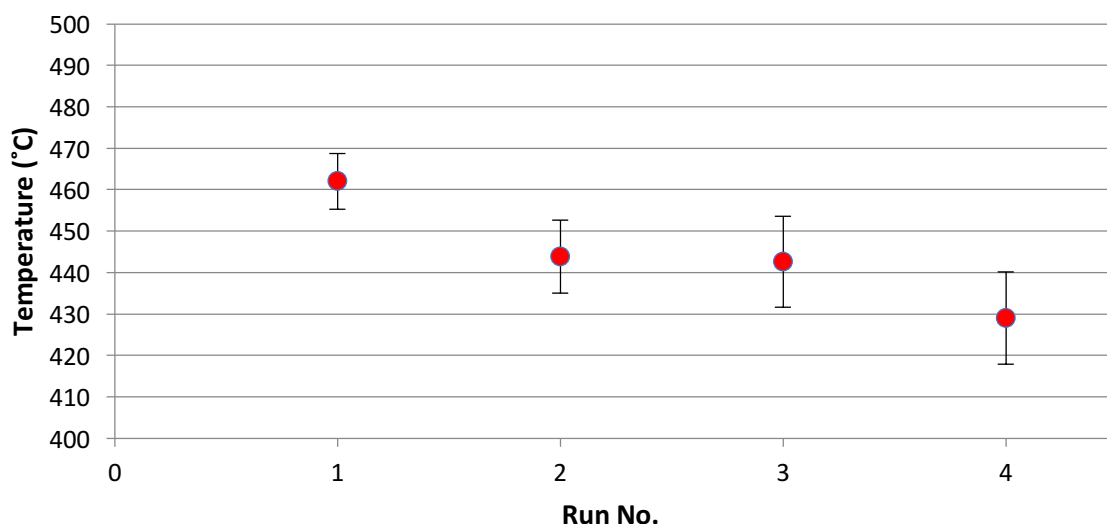


Figure 34: Threshold for emission for each Run averaged over all the samples, ARMo 9-13.

### 3.4 Trap Passivation Effect

#### 3.4.1 Theory

Traps are states in the gap between the conduction and the valence band. They are formed by structural, chemical or morphological defects in the crystal and exist as non-conductive states that vary in energetic and kinetic properties and limit charge mobility.<sup>57</sup> Crudely they are analogous to the existence of potholes in the conduction band.

It is posited that trap passivation – filling these “potholes” - enhances conductivity. The averaged emission results comparing  $\beta$  and non- $\beta$  over the experiments shows current density rising incrementally starting approximately half way through each Run (Figure 29). Emission should in theory plateau once the majority of unstable hydrogen sites have fully desorbed leaving only the higher work function temperature stable sites. It is postulated that this phenomenon is due to an increase in conductivity caused by trap passivation.

The NDNCD is considered a highly disordered semiconductor due to its high boundary-to-bulk ratio. Because of this the electric field induced from the 25 V bias over the 200 micron gap combined with the thermally induced current will progressively fill the traps. Once the trap sites are filled additional excited electrons will exist in the conduction band.<sup>58</sup> Figure 35 depicts how the trap passivation effect only becomes apparent once the rate of desorption stabilizes. Thereafter it is this effect which causes the increase in current produced in the latter stages of each Run.<sup>59</sup>

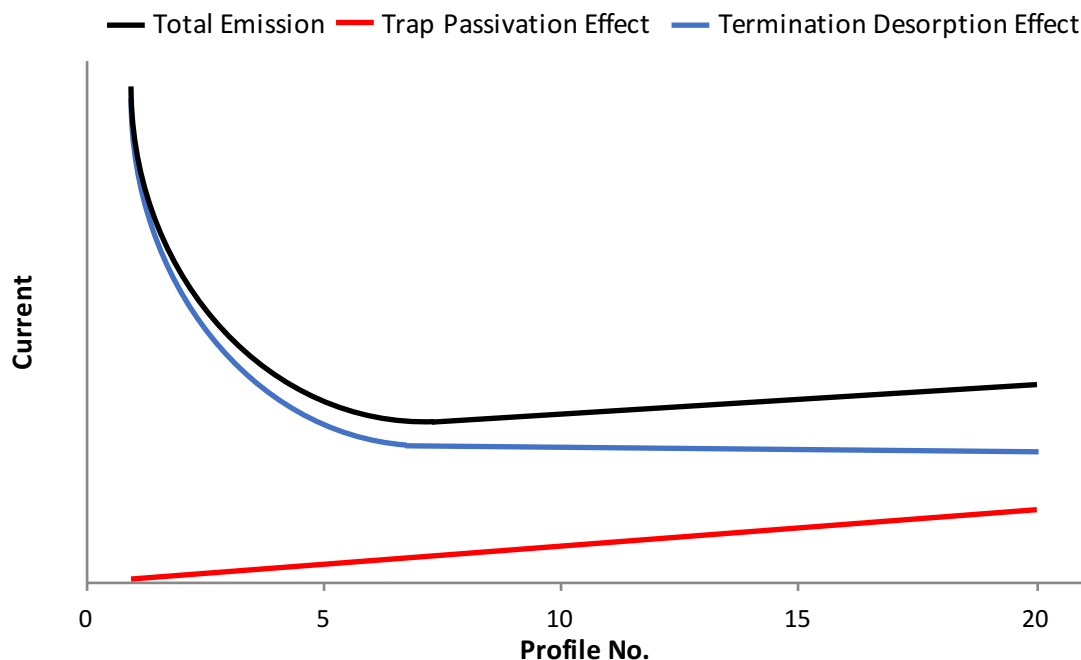


Figure 35: Schematic of the potential effect of trap passivation on the overall emission.

Using data from the comparative Runs, Figure 36 lends credence to this theory. When  $^{59}\text{Ni}$  is used there is a small (6%) increase in current density achieved by the end of the Run. When  $^{63}\text{Ni}$  is used this effect triples creating an 18% increase.

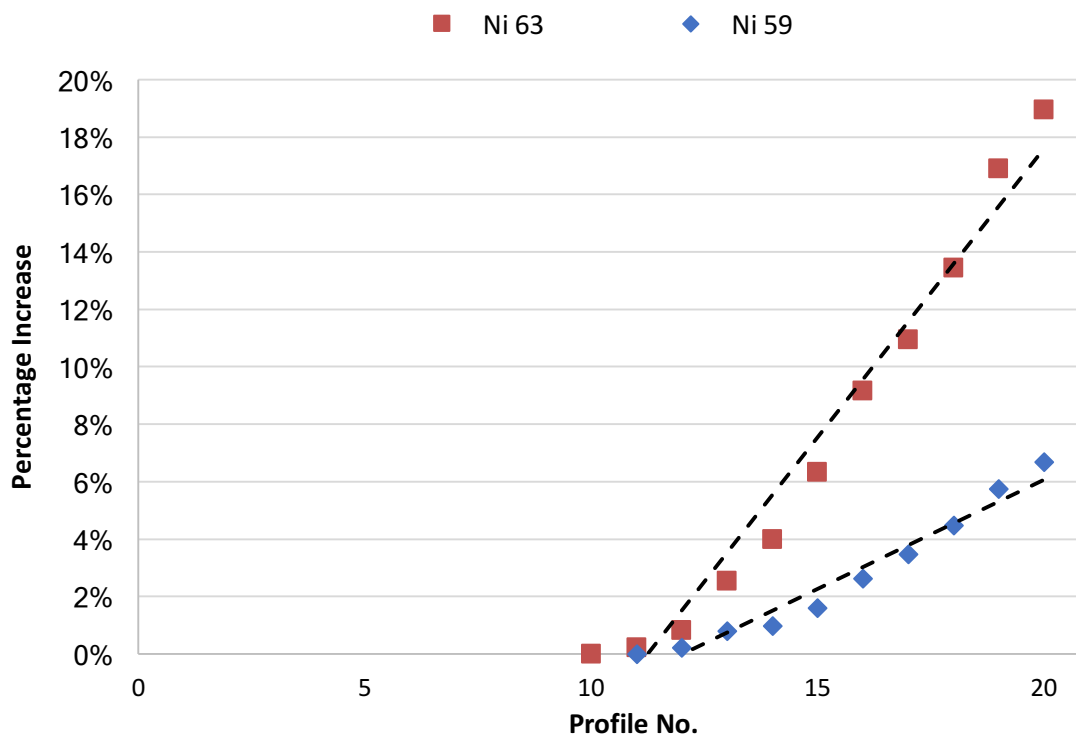


Figure 36: The percentage increase in peak emission with respect to the minimum measurement from the comparative Runs. The desorption dominated profiles, with decreasing emission, have been omitted for clarity.

### 3.4.2 Experimental

To test this theory a further experiment using the reserve emitter (ARMo 14) was undertaken. This emitter was terminated and a Run performed under identical conditions with  $^{59}\text{Ni}$  and  $^{63}\text{Ni}$  until the emission plateaued. Still held under vacuum, it was then Run a further three times (A to C) without retermination. Between each Run a 20-minute rest phase was introduced, with the bias off, to allow trapped electrons to recombine.

### 3.4.3 Results

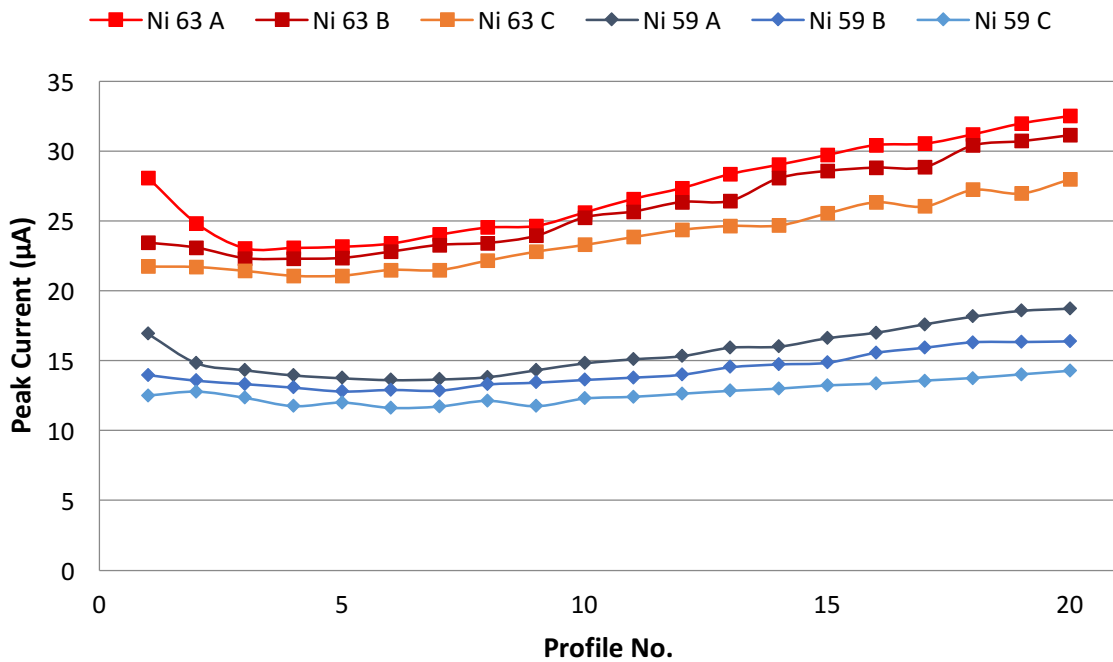


Figure 37: Comparison of the three sequential  $\beta$  and non- $\beta$  Runs of ARMo 14 without retermination.

The results generated are shown in Figure 37. The  $^{63}\text{Ni}$  Runs yield double the emission compared to  $^{59}\text{Ni}$ . The lack of retermination minimises the desorption effect allowing the passivation effect to become apparent much earlier in the Run. As expected, this came at the cost of greatly reduced emission but with improved stability across the Run. There is still an emission drop over the initial profiles (particularly evident in Run A). The sequential decrease from Runs A to C is minor but shows that the termination is still volatile.

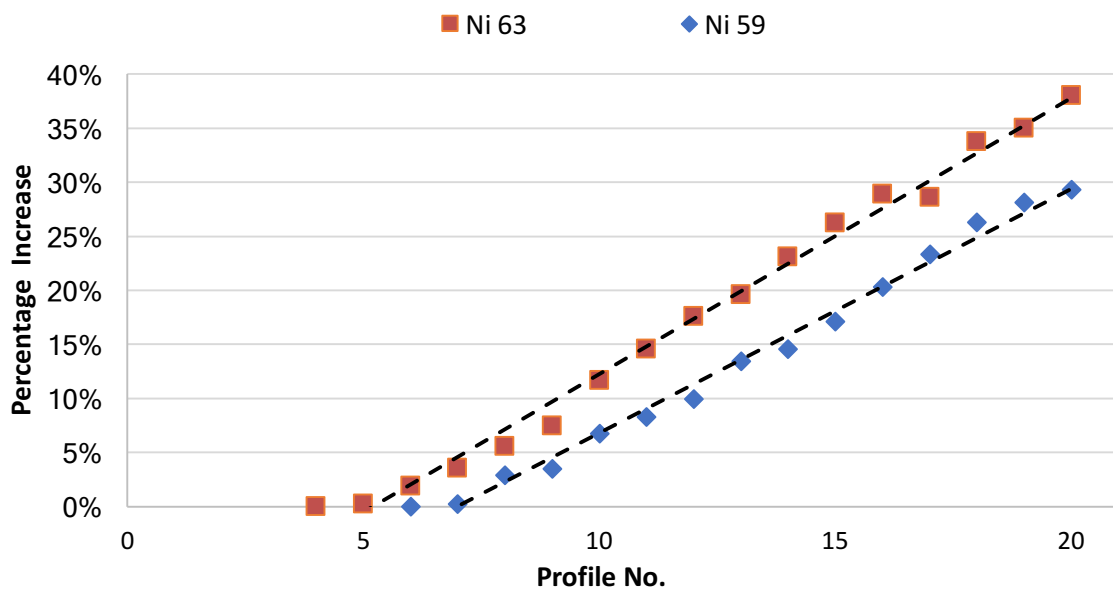


Figure 38: The percentage increase in peak emission normalised to the minimum measurement from the ARMo 14 Runs. The desorption dominated profiles, with decreasing emission, have been omitted for clarity.

Figure 38 indicates that the trap passivation effect is accelerated by beta irradiation as it is seen earlier in the Run and the steeper gradient indicates an increased rate of passivation thereafter. The combined effect of faster trap passivation and the lower resistance in the bulk gives support to the theory that beta irradiation enhances thermionic emission *via* RIC in beta generated channels.

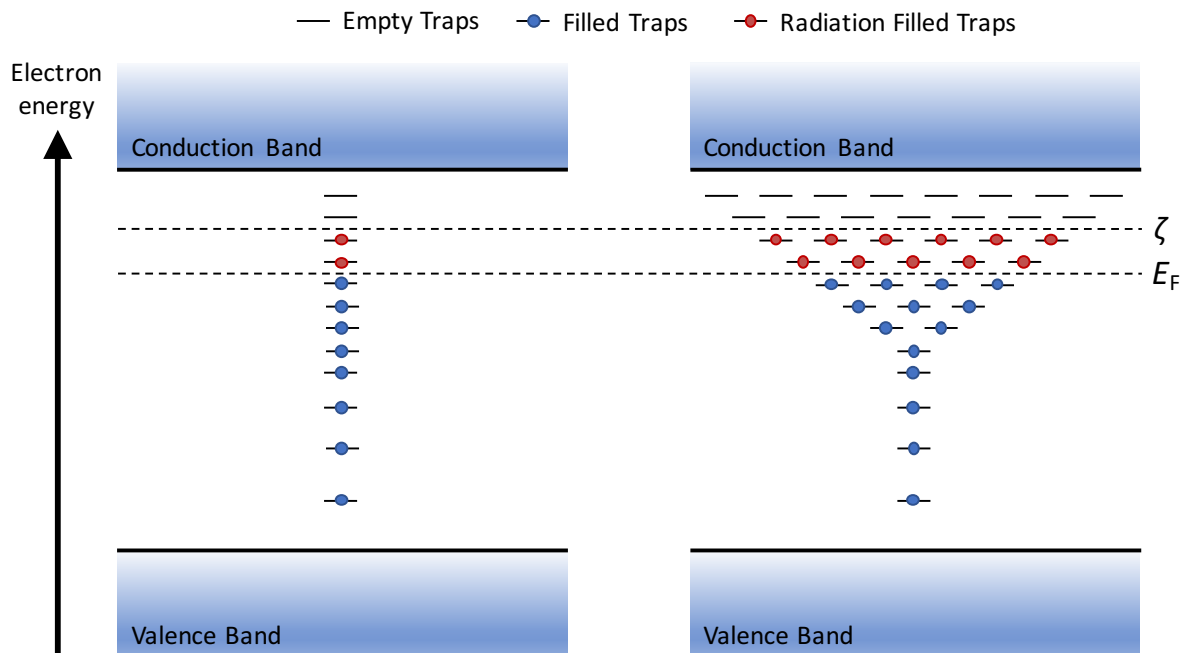


Figure 39: Potential diagram for a disordered n-type semiconductor under irradiation showing (Left) uniform and (Right) exponential energy distribution of localized trap states. Adapted from *Dennison et al.*<sup>60</sup>

This can be seen diagrammatically in Figure 39. The deposition of energy by the ionizing radiation raises the Fermi level,  $E_F$ , to the beta radiation induced quasi Fermi level,  $\zeta$ . The EHPs generated along the path of incident beta particle not only enhances conductivity by increasing the quantity of free charge carriers but also lowers the number of empty trap states again increasing conductivity.

## 4 Conclusion

### 4.1.1 Summary

Beta irradiation has been demonstrated to enhance thermionic emission. An increase in current density in excess of 100 % was consistently achieved using 2.6 MBq  $^{63}\text{Ni}$  source under experimental conditions. Of the three potential causes of BETE, radiation-induced conductivity remains the only viable explanation of this enhancement. Secondary emission will occur but can only account for a fraction of the emission augmentation.

The emission threshold was seen to decrease over the course of sequential Runs. This indicated an increase in the density of low work function sites caused from the regeneration of the termination of the emitters. No correlation was found between the emission threshold and the peak emission.

The increase in emission seen in the latter stages of the Runs has been posited to be an effect of trap passivation. This effect appears to be linear but the magnitude of the increase is emitter dependant. The beta enhancement of this effect provides support for the theory of RIC by using trap passivation as proxy for conductivity.

### 4.1.2 Future Work

BETE has been confirmed as a phenomenon. Future research should first aim to determine how, and then by how much beta irradiation can enhance thermionic emission. The posited theory of RIC should be tested with high temperature Hall effect and four-point probe measurements, elucidating the effects of irradiation on the conductivity of the n-type semiconductor.

$$\sigma_{RIC} = k_{RIC}D^{\Delta} \quad (6)$$

Equation 6 gives a theorised relationship between the conductivity,  $\sigma_{RIC}$ , and the absorbed dose rate,  $D$ , of radiation.  $k_{RIC}$  and  $\Delta$  are material and temperature dependant modifiers.<sup>60</sup> If RIC is confirmed this equation produces three areas for future investigation:

#### 1. The Radiation

The absorbed dose rate is the absorbed energy per unit mass. The nickel source used in this project was relatively weak in both activity (2.6 MBq with an approximate 1.3 MBq effective activity) and in energy ( $E_{\beta(\text{avg})} = 17.5$  keV). Given the scale of the current augmentation seen with this low dose rate, the potential for further enhancement should be investigated by repeating the experiments with varying activities of  $^{63}\text{Ni}$  sources and varying the source material to provide higher and lower energy betas (e.g.  $^{45}\text{Ca}$  whose  $E_{\beta(\text{avg})} = 254$  keV). Other forms of radiation such as gamma could also be considered for future enhancements.

## 2. The Temperature

The dependence of thermionic emission on temperature is well documented. The temperature dependence of beta enhancement is not. A relationship between temperature and RIC has been found in organic polymers but is posited to be caused by structural phase transitions in the material.<sup>59</sup> The temperatures required for phase transitions in diamond far exceed those used in this project, and any further research into BETE must establish what, if any, the relationship is.

## 3. The Material

The suitability of diamonds for beta augmentation is evident. However there is considerable scope for research within this area. The dopant concentration and type should be explored to further optimise the n-type semiconductor. Varying thickness of the diamond film and the diamond size from ultrananocrystalline to single crystal would help ascertain the effect of composition on conductivity. This would be highly beneficial for investigating not only thermionic emission but also the trap passivation effect and RIC. The experiments should also be repeated with p-type dopants to examine the effect of beta radiation on a semiconductor with a different majority charge carrier.

Further  $^{14}\text{C}$  should be considered as the future material for BETE. A diamond emitter fabricated out of  $^{14}\text{C}$ , would reduce the complexity of a beta enhanced system by integrating the beta source with the bulk. Ultimately this could considerably improve the viability of thermionic emission as a method of power generation.

Table 8: Radioactive properties of  $^{14}\text{C}$ .

Radioisotope $^{14}\text{C}$	
$\tau_{1/2}$ (annum)	5,730
$\beta$ Radiopurity (%)	100
$E_{\beta(\text{avg})}$ (keV)	49.5
$E_{\beta(\text{max})}$ (keV)	156.4



Table 8 and Equation 7 show the capacity for  $^{14}\text{C}$  to combine both source and emitter. A 1  $\mu\text{m}$  thick, 1  $\text{cm}^2$  nitrogen doped  $^{14}\text{C}$  diamond emitter would have an activity of 5.8 MBq, with a half-life of over 5000 years, with its dopant density increasing over time.

The  $^{14}\text{C}$  would be sourced from the considerable global stock pile of used graphite control rods, a waste product of nuclear power. This could enable TECs to reach efficiencies that make thermionic emission a viable technology for power generation with immediate potential application of BETE to augment PETE and non-terrestrial TECs.

## 6 Bibliography

---

- <sup>1</sup> W. Schlichter, *Annalen der Physik*, 1915, 352, 573-640.
- <sup>2</sup> G. Miskolczy and D. Lieb, *Proceedings of the 25th Intersociety Energy Conversion Engineering Conference*, 1990.
- <sup>3</sup> S. Riffat and X. Ma, *Applied Thermal Engineering*, 2003, 23, 913-935.
- <sup>4</sup> G. Snyder and T. Ursell, *Physical Review Letters*, 2003, 91.
- <sup>5</sup> G. Bennett, L. Lombardo, R. Hemler and J. Peterson, *Proceedings of the 21st Intersociety Energy Conversion Engineering Conference*, 1986.
- <sup>6</sup> G. Smestad, *Solar Energy Materials and Solar Cells*, 2004, 82, 227-240.
- <sup>7</sup> J. Schwede, T. Sarmiento, V. Narasimhan, S. Rosenthal, D. Riley, F. Schmitt, I. Bargatin, K. Sahasrabudhe, R. Howe, J. Harris, N. Melosh and Z. Shen, *Nature Communications*, 2013, 4, 1576.
- <sup>8</sup> J. Schwede, I. Bargatin, D. Riley, B. Hardin, S. Rosenthal, Y. Sun, F. Schmitt, P. Pianetta, R. Howe, Z. Shen and N. Melosh, *Nature Materials*, 2010, 9, 762-767.
- <sup>9</sup> K. Abdul Khalid, T. Leong and K. Mohamed, *IEEE Transactions on Electron Devices*, 2016, 63, 2231-2241.
- <sup>10</sup> N. Rasor, *Proceedings of the IEEE*, 1963, 51, 733-747.
- <sup>11</sup> S. Basu, Z. Zhang and C. Fu, *International Journal of Energy Research*, 2009, 33, 1203-1232.
- <sup>12</sup> J. Lee, I. Bargatin, N. Melosh and R. Howe, *Applied Physics Letters*, 2012, 100, 173904.
- <sup>13</sup> G. Fitzpatrick, J. Koester, J. Chang, E. Britt and J. McVey, *Proceedings of the 31st Intersociety Energy Conversion Engineering Conference*, 1996.
- <sup>14</sup> F. Koeck and R. Nemanich, *Diamond and Related Materials*, 2009, 18, 232-234.
- <sup>15</sup> F. Koeck and R. Nemanich, *Journal of Applied Physics*, 2012, 112, 113707.
- <sup>16</sup> W. Paxton, M. Howell, W. Kang and J. Davidson, *Journal of Vacuum Science & Technology B, Nanotechnology and Microelectronics: Materials, Processing, Measurement, and Phenomena*, 2012, 30, 021202.
- <sup>17</sup> W. Paxton, A. Steigerwald, M. Howell, N. Tolk, W. Kang and J. Davidson, *Applied Physics Letters*, 2012, 101, 243509.
- <sup>18</sup> J. Smith, R. Nemanich and G. Bilbro, *Diamond and Related Materials*, 2006, 15, 870-874.
- <sup>19</sup> M. Dundek, *Diamonds*, 1st edn., 2011.
- <sup>20</sup> G. Klein, *Faceting history*, 1st edn., 2005.
- <sup>21</sup> P. May, *Philosophical Transactions of the Royal Society A: Mathematical, Physical and Engineering Sciences*, 2000, 358, 473-495.
- <sup>22</sup> Chung, D, *Materials for electronic packaging*. 1st edn., 1995, 319-338.
- <sup>23</sup> J. Angus, H. Will and W. Stanko, *Journal of Crystal Growth*, 1968, 3-4, 172.
- <sup>24</sup> R. Sussmann, *CVD diamond for electronic devices and sensors*, J. Wiley, Chichester, U.K., 1st edn., 2009.
- <sup>25</sup> Z. Yiming, F. Larsson and K. Larsson, *Theoretical Chemistry Accounts*, 2013, 133.
- <sup>26</sup> S. Koizumi, T. Teraji and H. Kanda, *Diamond and Related Materials*, 2000, 9, 935-940.
- <sup>27</sup> D. Segev and S. Wei, *Physical Review Letters*, 2003, 91.
- <sup>28</sup> Y. Jiao, A. Hellman, Y. Fang, S. Gao and M. Käll, *Scientific Reports*, 2015, 5, 11374.
- <sup>29</sup> F. Wang, *Impurity doping processes in silicon*, 1st edn., 1981.
- <sup>30</sup> P. Lurie and J. Wilson, *Surface Science*, 1977, 65, 453-475.
- <sup>31</sup> B. Pate, *Surface Science*, 1986, 165, 83-142.

- 
- <sup>32</sup> Z. Zhang and J. Yates, *Chemical Reviews*, 2012, 112, 5520-5551.
- <sup>33</sup> J. Boeyens and J. du Toit, *Electronic Journal of Theoretical Chemistry*, 1997, 2, 296-301.
- <sup>34</sup> L. Diederich, O. Küttel, P. Aebi and L. Schlapbach, *Surface Science*, 1998, 418, 219-239.
- <sup>35</sup> J. Rameau, J. Smedley, E. Muller, T. Kidd and P. Johnson, *Physical Review Letters*, 2011, 106.
- <sup>36</sup> V. Seshan, D. Ullien, A. Castellanos-Gomez, S. Sachdeva, D. Murthy, T. Savenije, H. Ahmad, T. Nunney, S. Janssens, K. Haenen, M. Nesládek, H. van der Zant, E. Sudhölter and L. de Smet, *The Journal of Chemical Physics*, 2013, 138, 234707.
- <sup>37</sup> G. Kern, J. Hafner and G. Kresse, *Surface Science*, 1996, 366, 445-463.
- <sup>38</sup> Z. Zhang, M. Wensell and J. Bernholc, *Physical Review B*, 1995, 51, 5291-5296.
- <sup>39</sup> P. Baumann and R. Nemanich, *Surface Science*, 1998, 409, 320-335.
- <sup>40</sup> B. Rezek, C. Sauerer, C. Nebel, M. Stutzmann, J. Ristein, L. Ley, E. Snidero and P. Bergonzo, *Applied Physics Letters*, 2003, 82, 2266.
- <sup>41</sup> L. Diederich, P. Aebi, O. Küttel and L. Schlapbach, *Surface Science*, 1999, 424, L314-L320.
- <sup>42</sup> D. Takeuchi, S. Ri, H. Kato, C. Nebel and S. Yamasaki, *Physica Status Solidi (a)*, 2005, 202, 2098-2103.
- <sup>43</sup> A. Shih, J. Yater, C. Hor and R. Abrams, *Applied Surface Science*, 1997, 111, 251-258.
- <sup>44</sup> A. Shih, J. Yater, P. Pehrsson, J. Butler, C. Hor and R. Abrams, *Journal of Applied Physics*, 1997, 82, 1860-1867.
- <sup>45</sup> S. Wang, Q. Zhang, S. Yoon, J. Ahn, Q. Zhou, Q. Wang, D. Yang, J. Li and S. Zhang Shanyong, *Surface and Coatings Technology*, 2003, 167, 143-147.
- <sup>46</sup> F. Köck, J. Garguilo and R. Nemanich, *Diamond and Related Materials*, 2004, 13, 1022-1025.
- <sup>47</sup> F. Koeck and R. Nemanich, *Diamond and Related Materials*, 2006, 15, 217-220.
- <sup>48</sup> M. Suzuki, T. Ono, N. Sakuma and T. Sakai, *Diamond and Related Materials*, 2009, 18, 1274-1277.
- <sup>49</sup> F. Koeck and R. Nemanich, *Diamond and Related Materials*, 2009, 18, 232-234.
- <sup>50</sup> Alex Croot, personal communication, 2017.
- <sup>51</sup> S. Nunez-Sanchez, H. Andrade, C. Harwood, I. Bickerton, N. Fox, and M. Cryan, *The 6th International Conference on Metamaterials, Photonic Crystals and Plasmonics*, 2015.
- <sup>52</sup> S. Praver, K. Nugent, D. Jamieson, J. Orwa, L. Bursill and J. Peng, *Chemical Physics Letters*, 2000, 332, 93-97.
- <sup>53</sup> H. Kuzmany, R. Pfeiffer, N. Salk and B. Günther, *Carbon*, 2004, 42, 911-917.
- <sup>54</sup> H. D. Andrade, PhD thesis, University of Bristol, 2017
- <sup>55</sup> V. Robinson, Y. Show, G. Swain, R. Reifenberger and T. Fisher, *Diamond and Related Materials*, 2006, 15, 1601-1608.
- <sup>56</sup> I. Lin, S. Koizumi, J. Yater and F. Koeck, *MRS Bulletin*, 2014, 39, 533-541.
- <sup>57</sup> J. Dacuña and A. Salleo, *Physical Review B*, 2011, 84.
- <sup>58</sup> J. Montero, J. Bisquert, G. Garcia-Belmonte, E. Barea and H. Bolink, *Organic Electronics*, 2009, 10, 305-312.
- <sup>59</sup> S. Olthof, S. Singh, S. Mohapatra, S. Barlow, S. Marder, B. Kippelen and A. Kahn, *Applied Physics Letters*, 2012, 101, 253303.
- <sup>60</sup> J. Dennison, J. Gillespie, J. Hodges, R. Hoffmann, J. Abbott, S. Hart, A. Hunt, F. McDaniel and B. Doyle, *AIP Conference Proceedings*, 2009.